



Research Internship (PRe)

Field of Study: Fluid Interfaces and Computational Fluid Mechanics

Scholar Year: 2020-2021

Bubble Rise Dynamics in a Field of Varying Gravity

Confidentiality Notice

Non-confidential report and publishable on Internet

Author:

Pedro Morel Rosa

ENSTA Paris Tutor:

Marica Pelanti

Promotion:

2022

Host Organism Tutor:

Laurent Duchemin

Anne Mongruel

Internship from 17/05/2021 to 18/08/2021

Name of the host organism: PMMH - ESPCI

Address: 7 Quai Saint-Bernard

Paris

France

Confidentiality Notice

This present document is not confidential. It can be communicated outside in paper format or distributed in electronic format.

Abstract

This work aims to complement the understanding of the rise of bubble dynamics in reorientation studies. In particular, how the added mass force varies with different confinements and initial bubble shapes.

In order to achieve these results, concepts and validations relevant to the area of interface dynamics are presented under a theoretical and numerical perspective. Furthermore, the open-source *Basilisk* tool is used and its adaptive refinement method based on meshes in octrees is also presented.

Keywords: interfacial dynamics, computational methods, bubbles, reorientation, Basilisk, varying gravity, added mass.

Résumé

Ce travail vise à compléter la compréhension de la montée de la dynamique des bulles dans les études de réorientation. En particulier, comment la force de masse ajoutée varie avec différents confinements et formes de bulles initiales.

Afin d'atteindre ces résultats, des concepts et des validations pertinents pour le domaine de la dynamique des interfaces sont présentés sous une perspective théorique et numérique. De plus, l'outil open-source *Basilisk* est utilisé et sa méthode de raffinement adaptatif basée sur des maillages en octrees est également présentée.

Mots-clés: dynamique interfaciale, méthodes numériques, bulles, réorientation, Basilisk, gravité variable, masse ajoutée.

Acknowledgements

O presente é tão grande, não nos afastemos. Não nos afastemos muito, vamos de mãos dadas

The present is so large, let's not stray far. Let's stay together and go hand in hand
Carlos Drummond de Andrade, *Mãos Dadas*

This work, as well as my studies in Brazil and France, would never be possible without the people I love, whose unconditional support is indifferent to distance.

I give heartfelt thanks to everyone in my family, those who live and stand by my side, and those who are no longer there but whose teachings and memories I will carry forever.

I also thank my friends in Brazil and France, without whom daily life would be less easy. To everyone, thank you, obrigado.

To all my fellow students at the Universidade Federal do Rio de Janeiro (UFRJ), with whom I learned a lot.

I express my gratitude to my research supervisors, Laurent Duchemin and Anne Mongruel, for the opportunity and mentoring.

To every teacher I have had in life, since the very beginning of my education until now, I can not thank you enough.

*Dedicated to my grandfather,
who passed during the beginning of this summer internship.*

Contents

Confidentiality Notice	2
	3
Acknowledgements	4
Contents	6
Introduction	8
1 Interfacial Dynamics and Computational Methods	9
1.1 Introduction	9
1.2 Equations	9
1.2.1 Incompressible two-phase flows	9
1.2.2 Nondimensionalization	10
1.3 Physical and Theoretical Perspectives	12
1.3.1 Nondimensional Numbers	12
1.3.2 The Rising Bubble Phase Plot	12
1.3.3 Breakup Regimes	13
1.4 Computational Aspects	15
1.4.1 Numerical Set-Up	15
1.4.2 <i>Basilisk</i> 's Grid Adaptation Algorithm	16
2 Validation	18
2.1 Introduction	18
2.2 Stokes Flow	18
2.2.1 Theory	18
2.2.2 Simulation	19
2.3 Tripathi's Phase Plot	20
2.4 Taylor Bubbles	23
2.4.1 Theory	23
2.4.2 Simulations	25
3 Varying Gravity	30
3.1 Introduction	30
3.2 Gandikota's Experiment	30
3.3 Simulations	32

CONTENTS

4 Added Mass	34
4.1 Introduction	34
4.2 Theory	34
4.2.1 Physical Perspectives	34
4.2.2 Added Mass for Bubble Ascension	35
4.3 Simulations	35
4.3.1 Constant vs Varying Gravity	35
4.3.2 Aspect Ratio Study	36
4.3.3 Eccentricity Study	38
5 Conclusion	39
Bibliography	40
List of Tables	42
List of Figures	43

Introduction

Reorientation studies are focused on the analysis of confined gas/vapor bubbles rising inside a column of liquid due to fast variations of gravity. Its relevance, from an application perspective, is the performance optimization of liquid propulsion rocket systems; given that small accelerations (called reorientation accelerations) are used to collect the propellant at the inlet of the engine.

With this in mind, bubble dynamics in these studies differ from classical studies in 3 main axes: confinement effects, initially non-trivial bubble shapes, such as ellipses (due to the application of reorientation accelerations) and use of variable gravitational forces. Additionally, several theoretical reviews and validations of simpler bubble dynamics are carried out beforehand in order to establish a robust foundation of understanding.

Part 1 aims at exploring the theoretical and numerical aspects required to understand two-phase flow dynamics; specifically, in the case of bubble rise.

The purpose of Part 2 is to validate the numerical implementation. In order to achieve this, well-known dynamics for bubble rise, such as bubbles in Stokes regimes and Taylor bubbles, are discussed, simulated and compared to analytical results.

In part 3, the discussion related to reorientation studies begins. Gandikota's work [?] is presented, discussed and validated through simulations.

Finally, in part 4, with the theoretical background developed throughout the work, the concept of added mass is presented, in addition to being denoted in the case of rising bubbles. Furthermore, the added mass force is studied under different domain constraints and eccentricities for the initial elliptical shape of the bubble.

Part 1

Interfacial Dynamics and Computational Methods

1.1 Introduction

The goal of this section is to explore the theoretical and numerical aspects required to understand two-phase flow dynamics; specifically, in the case of bubble rise. Firstly, the incompressible Navier-Stokes equation for two-phase flow with variable gravitational term will be presented and nondimensionalized. Then, a brief discussion will follow regarding the dimensionless numbers in view of theoretical and experimental aspects for the rise of bubbles.

Given this discussion, the numerical implementation made in the *Basilisk* program will be explored. Notably, its discretization based on dynamic mesh refinement using quad/octrees, the schemes developed to operate on these structures and the methods used for handling the two-phase aspect of the problem.

1.2 Equations

1.2.1 Incompressible two-phase flows

For incompressible flows, one can state the following formulation for the conservation of mass (1.1) and momentum (1.2):

$$\vec{\nabla} \cdot \vec{u} = 0 \quad (1.1)$$

$$\rho \left[\frac{\partial(\vec{u})}{\partial t} + (\vec{u} \cdot \vec{\nabla}) \vec{u} \right] = -\vec{\nabla} p + \eta \Delta \vec{u} - \rho g(t) \vec{e}_z \quad (1.2)$$

In more detail, the varying gravitational field is defined in terms of a reference value, g_0 :

$$g(t) = g_0 f(t) \quad (1.3)$$

Taking this formulation into account, it is necessary to distinguish the intensive properties of each phase. For this purpose, subscript **1** will be used, for the liquid phase; and **2**, for the gas phase. Therefore, equation (1.2) can be divided in two:

$$\rho_1 \left[\frac{\partial(\vec{u})}{\partial t} + (\vec{u} \cdot \vec{\nabla}) \vec{u} \right] = -\vec{\nabla} p + \eta_1 \Delta \vec{u} - \rho_1 g(t) \vec{e}_z \quad (1.4)$$

$$\rho_2 \left[\frac{\partial(\vec{\mathbf{u}})}{\partial t} + (\vec{\mathbf{u}} \cdot \vec{\nabla}) \vec{\mathbf{u}} \right] = -\vec{\nabla} p + \eta_2 \Delta \vec{\mathbf{u}} - \rho_2 g(t) \vec{\mathbf{e}}_z \quad (1.5)$$

And considering the two-phase nature of the problem, an additional equation is required to take into account the surface tension forces between the different phases of the phenomenon; the Young-Laplace equation (1.6):

$$p_1 - p_2 = \gamma \kappa = \gamma \left(\frac{1}{R_1} + \frac{1}{R_2} \right) \quad (1.6)$$

1.2.2 Nondimensionalization

In order to obtain a more detailed understanding of the dynamics of the problem and to establish a coherent foundation between physical phenomenon and numerical simulation, it is necessary to nondimensionalize the equations (1.4), (1.5) and (1.6).

An initial analysis that can be done with the *Buckingham π Theorem* is finding the minimum amount of dimensionless parameters that can be obtained for an equivalent system of equations. In mathematical terms, one can start with a physically meaningful system such as $f(q_1, q_2, \dots, q_n) = 0$, where the q_i are n independent physical variables, and expressed in terms of k independent physical units. Then, this system can be restated as $F(\pi_1, \pi_2, \dots, \pi_k) = 0$; where the π_i are dimensionless parameters constructed from the q_i by $p = n - k$ dimensionless equations — the so-called π groups.

In this study, the system presents 7 independent physical variables ($\rho_1, \rho_2, \eta_1, \eta_2, R, g_0, \gamma$) and 3 independent physical units ([kg], [m], [s]). Therefore, one can expect the equivalence with a system described by 4 dimensionless parameters.

Initially, some choices are made to nondimensionalize the variables. In particular, the initial radius of the bubble R and the reference value for gravity g_0 are used. At first, the pressure is left with a term p_0 that will be conveniently chosen later.

$$\begin{cases} x = x^* R \\ u = u^* \sqrt{g_0 R} \end{cases} \quad \begin{cases} t = t^* \frac{\sqrt{R}}{g_0} \\ p = p^* p_0 \end{cases} \quad (1.7)$$

With that, the equivalences in (1.7) are initially applied to equation (1.4), the liquid phase.

$$\rho_1 g_0 \left[\frac{\partial(\vec{\mathbf{u}}^*)}{\partial t^*} + (\vec{\mathbf{u}}^* \cdot \vec{\nabla}^*) \vec{\mathbf{u}}^* \right] = -\frac{p_0}{R} \vec{\nabla}^* p^* + \frac{\eta_1 \sqrt{g_0 R}}{R^2} \Delta^* \vec{\mathbf{u}}^* - \rho_1 g_0 f(t) \vec{\mathbf{e}}_z$$

Dividing both sides by $\rho_1 g_0$ and choosing $p_0 = \rho_1 g_0 R$:

$$\left[\frac{\partial(\vec{\mathbf{u}}^*)}{\partial t^*} + (\vec{\mathbf{u}}^* \cdot \vec{\nabla}^*) \vec{\mathbf{u}}^* \right] = -\vec{\nabla}^* p^* + \frac{1}{Ga} \Delta^* \vec{\mathbf{u}}^* - f(t) \vec{\mathbf{e}}_z \quad (1.8)$$

Here, the Galilei number is denoted:

$$Ga = \frac{\rho_1 \sqrt{R g_0} R}{\eta_1} \quad (1.9)$$

And comparing equations (1.4) and (1.8), one can establish a perfect equivalence:

$$\rho_1^* \left[\frac{\partial(\vec{\mathbf{u}}^*)}{\partial t^*} + (\vec{\mathbf{u}}^* \cdot \vec{\nabla}^*) \vec{\mathbf{u}}^* \right] = -\vec{\nabla}^* \vec{p}^* + \eta_1^* \Delta^* \vec{\mathbf{u}}^* - \rho_1^* g^*(t) \vec{\mathbf{e}}_z \quad (1.10)$$

By conveniently choosing:

$$\begin{cases} \rho_1^* = 1 \\ \eta_1^* = \frac{1}{Ga} \\ g^*(t) = f(t) \end{cases} \quad (1.11)$$

The exact same process is applied to equation (1.5). First the equivalences in (1.7) are used, and then both sides are divided by $\rho_1 g_0$. Finally, we multiply and divide the diffusive term by η_1 :

$$\frac{\rho_2}{\rho_1} \left[\frac{\partial(\vec{\mathbf{u}}^*)}{\partial t^*} + (\vec{\mathbf{u}}^* \cdot \vec{\nabla}^*) \vec{\mathbf{u}}^* \right] = -\vec{\nabla}^* \vec{p}^* + \frac{\eta_2}{\eta_1} \frac{1}{Ga} \Delta^* \vec{\mathbf{u}}^* - \frac{\rho_2}{\rho_1} f(t) \vec{\mathbf{e}}_z$$

Expressing the ratios of the properties as $\rho_R = \frac{\rho_1}{\rho_2}$, $\eta_R = \frac{\eta_1}{\eta_2}$ and comparing equations (1.5) and (1.2.2):

$$\rho_2^* \left[\frac{\partial(\vec{\mathbf{u}}^*)}{\partial t^*} + (\vec{\mathbf{u}}^* \cdot \vec{\nabla}^*) \vec{\mathbf{u}}^* \right] = -\vec{\nabla}^* \vec{p}^* + \eta_2^* \Delta^* \vec{\mathbf{u}}^* - \rho_2^* g^*(t) \vec{\mathbf{e}}_z \quad (1.12)$$

By conveniently choosing:

$$\begin{cases} \rho_2^* = \frac{1}{\rho_R} \\ \eta_2^* = \frac{1}{\eta_R} \frac{1}{Ga} \\ g^*(t) = f(t) \end{cases} \quad (1.13)$$

Lastly, the Young-Laplace equation (1.6) needs to be nondimensionalized. Using the equivalences in (1.7) and the choice for p_0 :

$$p_1^* \rho_1 R g_0 - p_2^* \rho_1 R g_0 = \frac{\gamma \kappa^*}{R}$$

And multiplying both sides by $\rho_1 R g_0$:

$$p_1^* - p_2^* = \frac{\gamma}{\rho_1 R^2 g_0} \kappa^* \quad (1.14)$$

Comparing equations (1.6) and (1.14), one can establish once more the equivalence:

$$p_1^* - p_2^* = \gamma^* \kappa^* \quad (1.15)$$

And the Bond number can be denoted as:

$$Bo = \frac{\rho_1 R^2 g_0}{\gamma} \quad (1.16)$$

In a final analysis, it becomes evident that there is a well established equivalence between equations (1.4), (1.5), (1.6) and equations (1.10), (1.12), (1.15); respectively. Notably, the latter are formulated with 4 dimensionless parameters:

$$\begin{cases} Ga = \frac{\rho_1 \sqrt{Rg_0} R}{\eta_1} \\ Bo = \frac{\rho_1 R^2 g_0}{\gamma} \end{cases} \quad \begin{cases} \rho_R = \frac{\rho_1}{\rho_2} \\ \eta_R = \frac{\eta_1}{\eta_2} \end{cases} \quad (1.17)$$

1.3 Physical and Theoretical Perspectives

1.3.1 Nondimensional Numbers

In order to fully understand the influence of the Galilei and Bond numbers, it is necessary to analyze the equations (1.9) and (1.16); and highlight the physical parameters at play.

$$Ga = \frac{\rho_1 \sqrt{Rg_0} R}{\eta_1}$$

The Galilei number is the ratio of the gravitational force to the viscous force. It is interesting to note that the term $\sqrt{g_0 R}$ reflects the characteristic velocity of the bubble; that is, high values for the Galilei number imply more abrupt dynamics and transient phenomena of great complexity. Another valuable observation is the similarity of this dimensionless number to the Reynolds number; but with the advantage of not presenting an explicit velocity term, since the bubble may not reach a terminal dynamic.

$$Bo = \frac{\rho_1 R^2 g_0}{\gamma}$$

Similarly, the Bond number expresses the ratio of gravitational forces to surface tension forces. This means that high values for the Bond number reflect the high deformability of the bubble due to the dynamics of its ascension. It is equally interesting to note the similarity between this dimensionless number and Weber's number; with the same advantage of not having an explicit velocity term. It can also be called Eötvös number (Eo).

1.3.2 The Rising Bubble Phase Plot

In recent studies, Tripathi et al. (2015) [1] showed the relevance of these two dimensionless numbers in bubble dynamics through numerical 3D simulations. Among the observed phenomena, he noted regimes in which the bubble exhibits path instability, chaotic motion, peripheral breakage of bubble structure, central breakage of bubble structure (which corresponds to a topological change for a toroid); just to name a few patterns.

Using the density ratio and the viscosity ratio as being $\rho_R = 1000$ and $\mu_R = 100$, respectively; he showed 5 different behavior patterns by varying the Galilei number between 0 and 700; and Bond between 0 and 500.

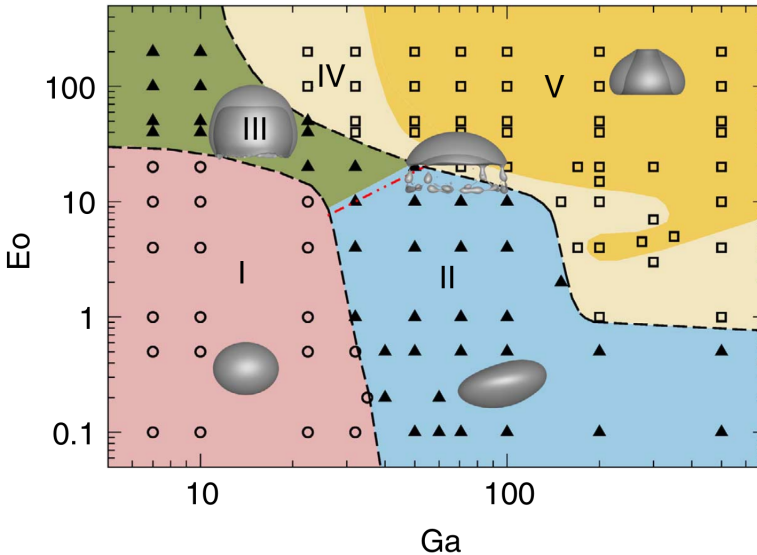


Figure 1.1: Different regimes of bubble shape and behaviour. Source: Tripathi et al. [1]

It is possible to distinguish the dynamic between three main behaviors: axisymmetric (circles); asymmetric (solid triangles); and breakup (squares).

The axisymmetric regime is called region I. The bubble retains its integrity and attains a constant ellipsoidal shape, with terminal velocity going straight upwards.

The two colors within the asymmetric regime represent non-oscillatory region III (shown in green), and oscillatory region II (blue) dynamics. In region III the bubble an axisymmetric cap with a thin skirt trailing the main body of bubble. Bubbles in this region travel upwards in a vertical line as well, and practically attain a terminal velocity after the initial transients. As for region II, bubbles display strong deviations from axisymmetry in this region, at relatively early times, and rise in a zigzag or a spiral manner.

Region IV is shown in light yellow colour, and region V is in dark yellow. The bubble, faced with higher gravity and relatively weak surface tension, breaks up or undergoes a change of topology in these regions. In region IV the bubble in this regime breaks into large axisymmetric spherical cap and several small satellite bubbles in the cap's wake; a phenomenon called "peripheral breakup". Finally, the bubbles shown in region V exhibit a "geyser" formation in the bottom centre, which leads to a change of topology: to a doughnut-like or toroidal shape.

1.3.3 Breakup Regimes

The dynamics presented in Fig. 1.1 are rich in details, being the subject of several studies ([2], [3], [4] [5], [6], [7], [8]). For the purpose of this specific work, it is interesting to have this general framework as a base, but the most relevant regimes will be the high Galilei and high Bond regimes - regions IV and V - where breakups occur.

At early times both bubbles are axisymmetric and present qualitatively very similar dynamics. The contrast between these two regimes is when the geyser (concave deformation at the base of the bubble) advances to the top of the bubble, causing the topological change and resulting in the toroid of region V; or backs off and forms a skirt, that then breaks off in the form of satellite bubbles - region IV. This evolution can be seen comparatively in Fig. 1.2.

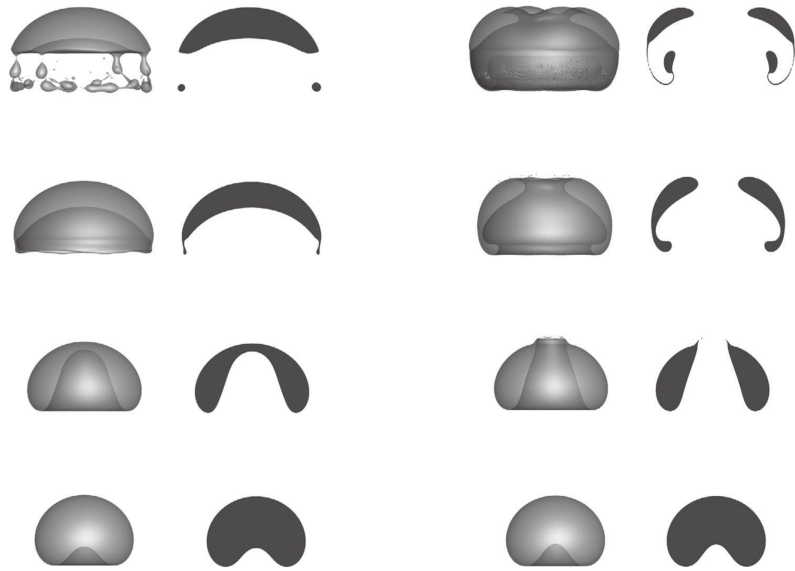


Figure 1.2: Time evolution of bubbles exhibiting a peripheral and a central breakup. Source: Tripathi et al. [1]

Considering the reasonably symmetrical nature of the dynamics of bubbles in the breakup regime, it is valid to question the necessity of 3D simulations rather than axisymmetric simulations. Indeed, there is a difference: while the axisymmetric simulations can only obtain breakup in the form of a ring that detaches from the spherical cap, 3D simulations enable the ejection of satellite bubbles, as it can be seen in Fig. 1.3. Another feature that the axisymmetric simulations will miss is the fact that the centre of gravity moves in the horizontal plane.



Figure 1.3: Differences between 2D and 3D bubble simulations from region IV. Source: Tripathi et al. [1]

This comment is highly relevant to the work, since **almost all simulations carried out in this study are axisymmetric** and will often have difficulty converging.

1.4 Computational Aspects

1.4.1 Numerical Set-Up

Throughout this work, the free software program Basilisk was used for the numerical simulations. Basilisk is a free-software that contains a second-order accurate finite-volume solver for the Navier–Stokes equations.

Among the implemented solvers, a centered Navier-Stokes formulation was chosen, along with the Volume-Of-Fluid (VOF) method. In detail, the scheme combines quad/octree discretisation, projection method and multilevel Poisson solver. Advection terms are discretised using the robust second-order upwind scheme of Bell, Colella and Glaz [9].

The VOF method is based on the idea of fraction function f . It is a scalar function, defined as the integral of a fluid's characteristic function in the control volume, namely the volume of a computational grid cell. The volume fraction of each fluid is tracked through every cell in the computational grid, while all fluids share a single set of momentum equations. When a cell is empty with no traced fluid inside, the value of f is zero; when the cell is full, $f = 1$; and when there is a fluid interface in the cell, $0 < f < 1$. f is a discontinuous function, its value jumps from 0 to 1 when the argument moves into interior of traced phase. The normal direction of the fluid interface is found where the value of f changes most rapidly. With this method, the free-surface is not defined sharply, instead it is distributed over the height of a cell. Thus, in order to attain accurate results, local grid refinements have to be done.

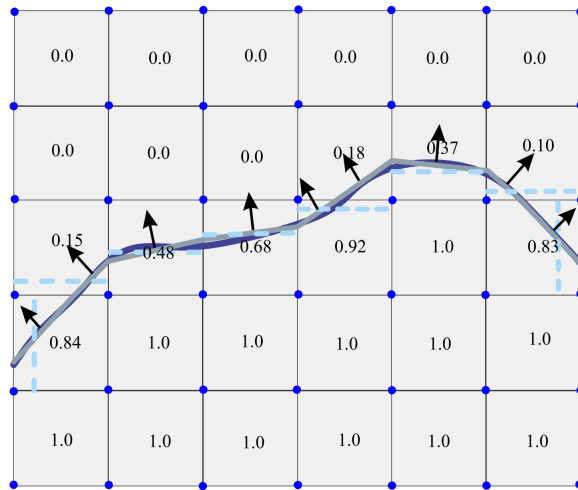


Figure 1.4: Schematic of fluid volume fraction and fluid interface. Source: Katopodes [10]

The evolution of the m -th fluid in a system on n fluids is governed by the transport equation :

$$\frac{\partial f_m}{\partial t} + \vec{u}^* \cdot \nabla f_m = 0 \quad (1.18)$$

With the following constraint :

$$\sum_{m=1}^n f_m = 1 \quad (1.19)$$

The particularities of the implementation are diverse and would fall outside the scope of details that this work intends to deal with. For a complete understanding of the methods it

is worth checking some articles that support exactly the implementation performed in Basilisk ([11], [12], [13]).

1.4.2 *Basilisk's Grid Adaptation Algorithm*

A characteristic of fluid flows is the very wide range of spatial scales often encountered: shocks in compressible flows, interfaces between immiscible liquids, turbulence intermittency and boundary layers are just a few examples. Consequently, in recent years a number of researchers have investigated the use of adaptive mesh refinement, where the spatial discretisation is adjusted to follow the scale and temporal evolution of flow structures.

Two main approaches have been developed: the hierarchical structured grid approach of Berger and Oliger (Adaptive Mesh Refinement, AMR) [14] and quad/octree based discretisations ([15], [16]). The AMR framework uses classical algorithms on regular Cartesian grids of different resolutions arranged hierarchically. The only modification necessary is to allow coupling between grids at different levels through the boundary conditions. Quad/octree discretisations, on the other hand, deal with various levels of refinement locally through the use of finite-difference operators adapted to work at fine/coarse cell boundaries.

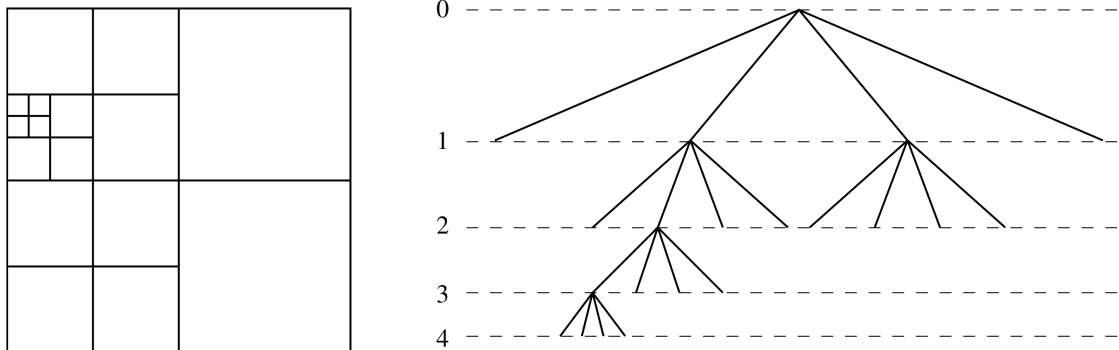


Figure 1.5: Example of quadtree discretisation and corresponding tree representation. Source: Popinet [11]

However, the refinement requires a decision algorithm. Basilisk's wavelet-based strategy is designed to be such an adaptation algorithm. In short, the adaptive wavelet algorithm is based around the estimation of numerical errors in the representation of spatially-discretized fields.

The `adapt_wavelet()` function requires the user to define a list of fields that will be analyzed for the refinement/coarsening. This list can consist of any combination of the existing scalar fields. In general, it makes sense to use the fields that appear in the equations that are being solved.

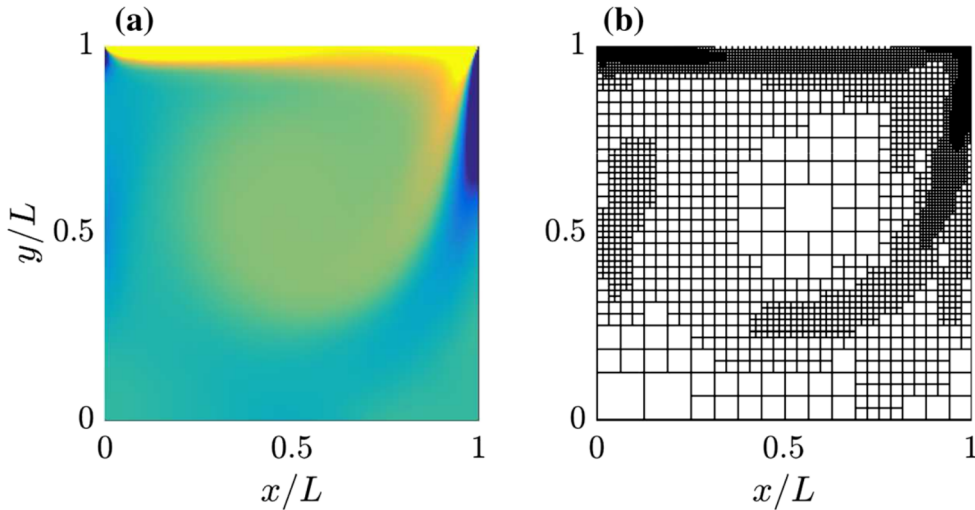


Figure 1.6: Example of octree refinement: snapshots of (a) the vorticity field, and (b) the numerical grid for the lid-driven cavity simulation with $Re_{lid} = 500$. Source: Van Hooft [17]

Additionally the maximum tolerated estimated error for each field needs to be defined. Finally, a maximum level (i.e. resolution) that the algorithm is allowed to employ should be provided. Optionally, two more inputs can be defined. i.e. 1: the minimum level of refinement and 2: A list of scalars that need to be updated. The default values of these optional arguments are 1 and all, respectively.

This means that with a simple command, the software gives the user the freedom to choose the scalar fields that will be taken into account for dynamic refinement.

More details about the nature of wavelet-based transformations, which are the basis of the mathematical rigor of the refinement decision algorithm, can be found in [17] and [18].

Part 2

Validation

2.1 Introduction

The purpose of this Part is to validate the numerical implementation. In order to achieve this, well-known dynamics for bubble rise, such as bubbles in Stokes regimes and Taylor bubbles, will be discussed, simulated and compared to analytical results. The different bubble dynamic regimes for the Tripathi phase diagram will also be simulated and compared.

Among these discussions, the qualitative discrepancy between 3D and axisymmetric simulations will be particularly highlighted and resources to remedy this discrepancy will be presented.

2.2 Stokes Flow

2.2.1 Theory

Stokes flow is a regime in which the inertial advective forces in the fluid flow are small compared to the viscous forces ($Re \ll 1$). In this theoretical framework, it is possible to consider the bubble as a solid with a static shape, ascending in the fluid medium by buoyancy. Conversely, there are opposing forces such as the weight and drag, counteracting the buoyancy.

$$F_{Buoyancy} = F_{Drag} + F_{Weight} \quad (2.1)$$

Considering the bubble as a perfect sphere, one can use the well known equation for Stokes drag to model the friction, in which V_t is the terminal velocity of the spherical bubble [19].

$$g \frac{4\pi R^3}{3} \rho_f = 4\pi \mu_f R V_t + g \frac{4\pi R^3}{3} \rho_g \quad (2.2)$$

Therefore, arranging accordingly:

$$V_t = \frac{1}{3} \frac{(\rho_f - \rho_g)}{\mu_f} g R^2 \quad (2.3)$$

If the simulation is performed correctly, the result is expected to be in accordance with this analytical expression. It has to be noted that at small Re number, hydrodynamic interactions between the sphere and the walls are long range. the size of the box may influence the results.

2.2.2 Simulation

As discussed in the 1.2 section, the physics of simulation can be set as a function of 4 dimensionless parameters. Among them is the density ratio ρ_R , the viscosity ratio μ_R , the Galilei number Ga and the Bond number Bo .

One can think of an experiment in which a fluid has a density $\rho_1 = 1000 \text{ kg/m}^3$ and a viscosity $\mu_1 = 10^{-3} \text{ Pa} \cdot \text{s}$, in which there is a bubble composed of fluid 2; with radius $R = 10^{-4} \text{ m}$, density $\rho_2 = 1 \text{ kg/m}^3$ and viscosity $\mu_2 = 10^{-3} \text{ Pa} \cdot \text{s}$. Local gravity is $g = 9.81 \text{ m/s}^2$. This setup was implemented based on classic experiments with bubbles in Stokes regime.

More formally, the dimensionless parameters of this experiment consist of:

- Density ratio $\rho_R = 1000$
- Viscosity ratio $\mu_R = 1000$
- Galilei number $Ga = 3.132$
- Bond number $Bo = 0.0014$

The Galilei and Bond numbers do reflect what is expected of this type of flow from a physical perspective. As the Galilei number is low, this denotes a strong influence of the viscous forces on the dynamics of the bubble's rise. Furthermore, the smallness of the Bond number reflects the fact that the bubble's deformability is practically null, remaining perfectly spherical over time. The latter can be seen consistently in Fig. 2.1.

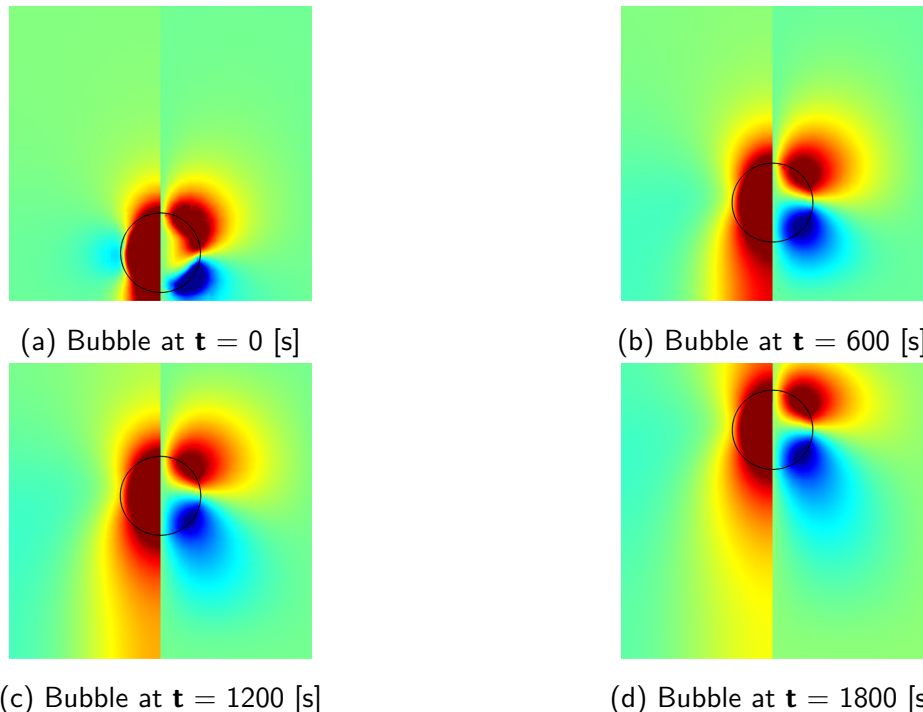


Figure 2.1: Snapshots of bubble ascending in Stokes flow. Vertical velocity on the left side and horizontal velocity on the right side.

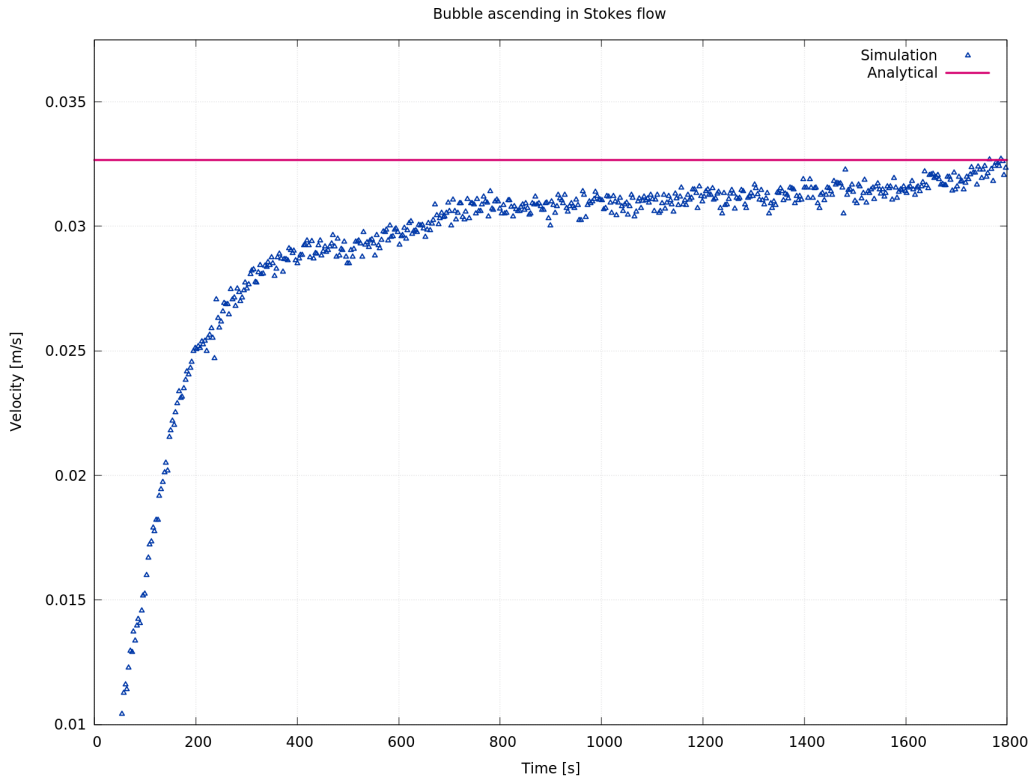


Figure 2.2: Comparison between analytical and numerical solution for bubble velocity in Stokes flow. Triangles : Numerical solution. Continuous line : Equation 2.3

And finally, in Fig. 2.2 , there is the comparative plot between the numerical results and the equation (2.3) for a bubble (or any spherical object) ascending in a stokes regime.

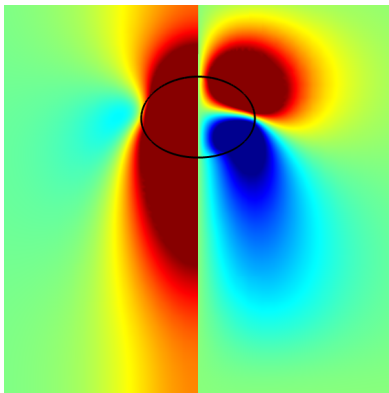
2.3 Tripathi's Phase Plot

Presented in subsection (1.3.2), it is of great interest to also validate the implementation in *Basilisk* using the results found in the rising bubble phase diagram (Fig. 1.1).

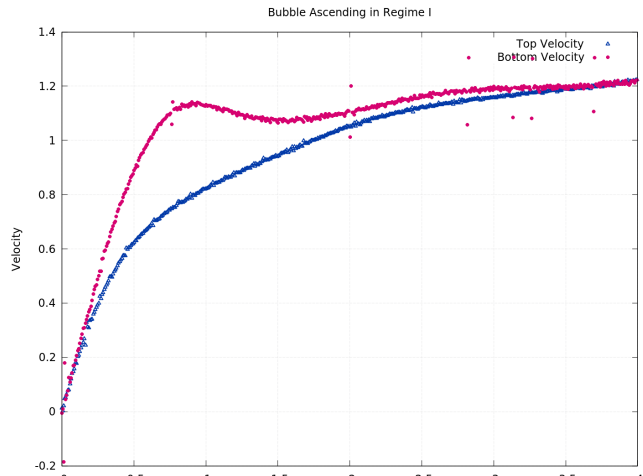
For this purpose, 5 values were chosen for the Galilei and Bond numbers based on the regions that present different dynamics in the diagram. Density and viscosity ratio values were fixed according to the article [1]; $\rho_R = 1000$ and $\mu_R = 100$, respectively. In Table 2.1, the Galilei and Bond values used to simulate each dynamic were listed.

	<i>Ga</i>	<i>Bo</i>
Region I	10	1
Region II	100	5
Region III	10	100
Region IV	30	100
Region V	200	100

Table 2.1: Galilei and Bond numbers used for each simulation based on the rising bubble phase plot.



(a) Snapshot of the bubble. Vertical velocity on the left and vorticity field on the right.



(b) Top and bottom velocity of the bubble.

Figure 2.3: Bubble ascending in regime I

For region I, the bubble is expected to reach a terminal velocity with an ellipsoidal shape. This becomes evident when analyzing Figs. 2.3a and 2.3b. Respectively, it is possible to see the ellipsoidal shape of the bubble in its terminal state; and the transient spherical to ellipsoidal deformation via the top and bottom velocities of the bubble.

For region II, with higher Bond and Galilei numbers, the dynamic seems to reach an unstable equilibrium. The bubble achieves neither form nor terminal velocity; oscillating along its ascent. This dynamic is notable through the analysis of Fig. 2.4.

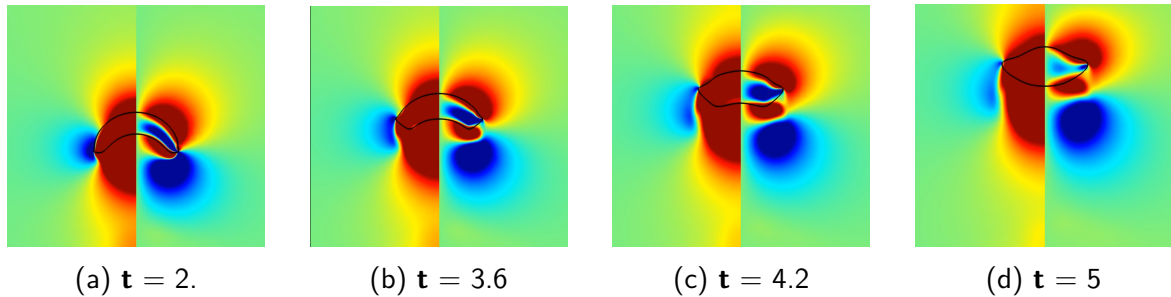
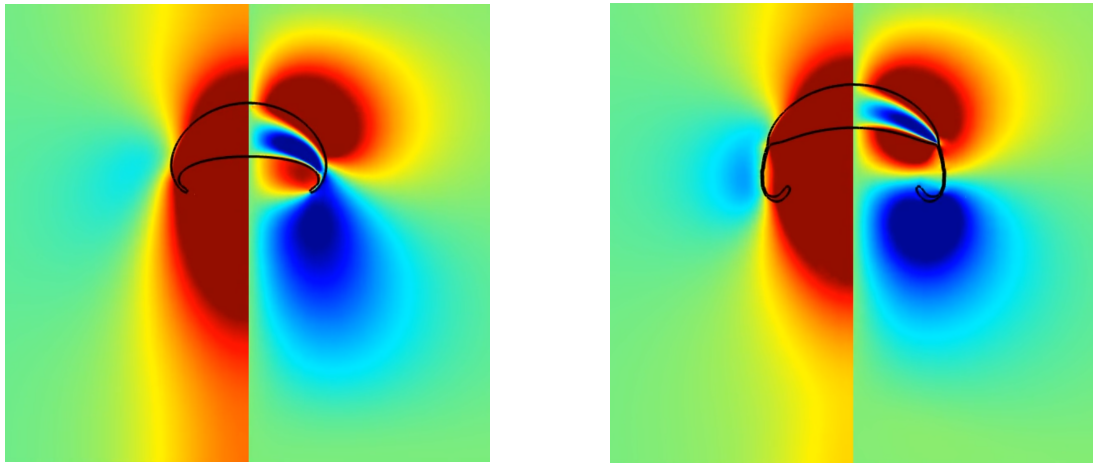


Figure 2.4: Oscillating behavior for bubble ascending in regime II. Vertical velocity on the left side and vorticity field on the right side.

Then, in region III, the bubble is expected to present an asymmetrical nature, with chaotic zigzag ascension patterns. Unfortunately, due to the axisymmetric nature of the simulation, this phenomenon could not be accurately represented. However, it is notable that the bubble has indeed the expected shape, with considerable concavity but not enough to generate a breakup (Fig. 2.5a).



(a) Bubble in regime III, without breakup. (b) Bubble in regime IV, almost breaking up.

Figure 2.5: Comparison between regimes III and IV. Vertical velocity on the left side and vorticity field on the right side.

As discussed in subsection (1.3.3), the bubbles belonging to region IV present the same mismatch between axisymmetric simulation and asymmetric nature. However, in Fig. 2.5b, it is possible to see the nature of the peripheral breakup, with the lateral flaps of the bubble forming a thin layer, on the verge of breaking up. Given this fact, the result found is perfectly equivalent to the results of the axisymmetric Tripathi simulation [1] (Fig. 1.3); not showing satellite bubble ejection.

Finally, reaching the highest values for the Galilei and Bond number of the Rising Bubble Phase Plot, region V presents abrupt dynamics, leading to the bubble's central breakup. This toroidal shape can be seen in Fig. 2.6, with the bubble contour remarkably disconnected from the axis of symmetry.

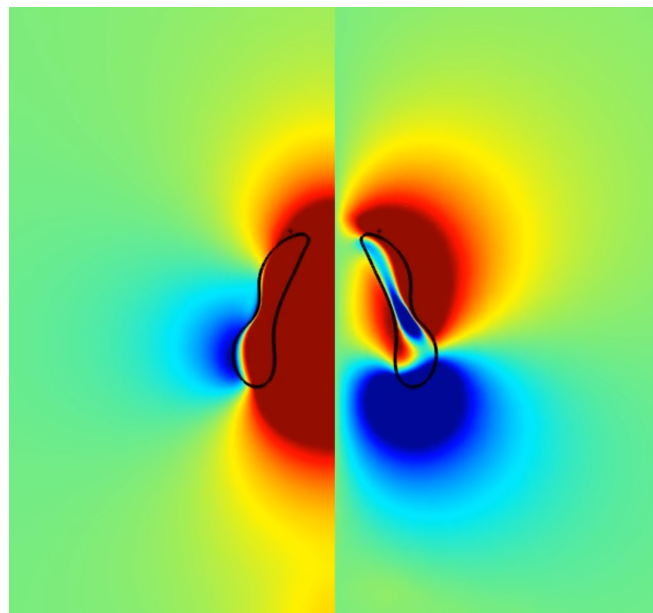


Figure 2.6: Toroidal bubble ascending in regime V. Vertical velocity on the left side and vorticity field on the right side.

2.4 Taylor Bubbles

2.4.1 Theory

Another benchmark of relevance in the study of bubble rise can be extracted from the results obtained by Taylor [20]. Peculiarly, the studied bubbles reach a terminal velocity, maintaining a spherical curvature at the top and a reasonably flat structure at the bottom.

In his study, he was able to establish an equation for terminal velocity U from a mechanistic perspective of the dynamics around the bubble.

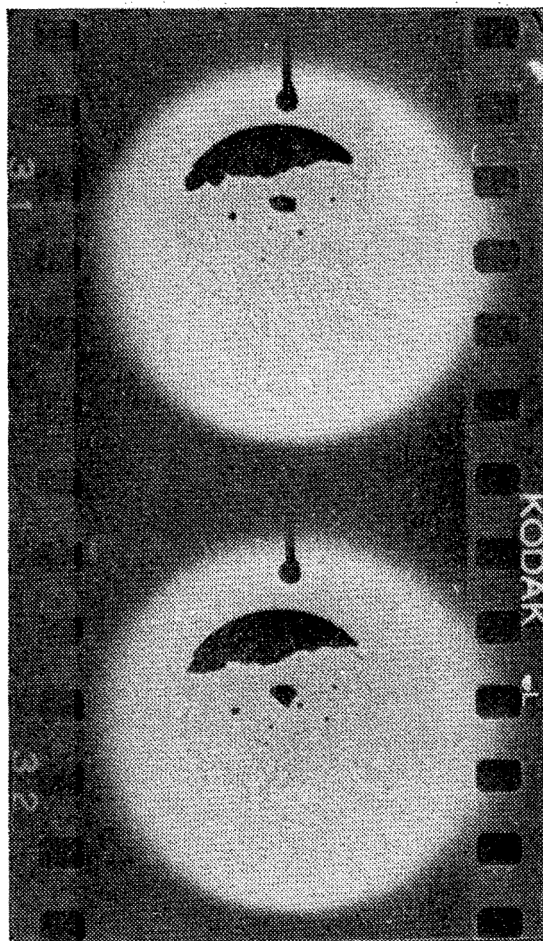


Figure 2.7: Experimental Taylor bubbles. Source: Davies and Taylor (1950) [20]

Starting from the information that the bubble is perfectly spherical at the top, the pressure on the top surface can be considered as uniform. The pressure in the fluid outside the bubble is due to the dynamics of the flow around it, and to gravity. The condition that the pressure at the surface of the bubble is uniform requires that these two causes shall neutralize each other. Applying Bernoulli's equation to steady flow relative to the bubble, and considering the relative velocity at its highest point as zero, the surface condition is:

$$q^2 = 2gx \quad (2.4)$$

Where x is the depth below the highest point, q the fluid velocity in the surface of the bubble and g is the acceleration of gravity.

In the high Re flow regime, the boundary layer thickness around the bubble is very thin. Therefore, the pressure distribution in the upper cap is quite similar to the theoretical pressure distribution using velocity potential theory. For this reason, using these classic results, one finds:

$$\frac{q^2}{U^2} = \frac{p_0 - p_\theta}{\frac{1}{2}\rho U^2} = \frac{9}{4} \sin^2 \theta \quad (2.5)$$

Here p_θ is the pressure at angle θ , p_0 that at the vertex and $\frac{1}{2}\rho U^2$ the dynamic pressure of the incident flow relative to the bubble.

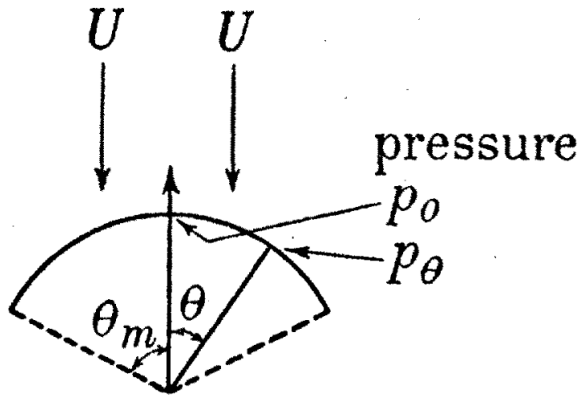


Figure 2.8: Scheme representing pressure variation with respect to the angle θ . Source: Davies and Taylor (1950) [20]

Furthermore, semi-spherical models made in brass with small pressure holes were used in a wind tunnel to measure the variation of pressure p_θ given an angle θ , as it can be seen in Fig. 2.8.

It can also be geometrically noted that the ratio x/R is equivalent to $1 - \cos \theta$, where R is the radius of the spherical surface of the lenticular body. This observation is rather relevant, because the experiments concluded that the values of the ratio $q^2/U^2(1 - \cos \theta)$ are approximately the same value.

Given these facts, one can use equation (2.5) as $q^2 = \frac{9}{4}U^2 \sin^2 \theta$, equation (2.4) as $q^2/x = 2g$ and the geometrical argument $x = R_C(1 - \cos \theta)$ to conclude for the stagnation point:

$$\frac{U^2}{gR_C} = \frac{8}{9} \left(\frac{1 - \cos \theta}{\sin^2 \theta} \right) \quad (2.6)$$

And when θ is small, $(1 - \cos \theta)/\sin^2 \theta \rightarrow \frac{1}{2}$:

$$U = \frac{2}{3} \sqrt{gR_C} \quad (2.7)$$

When compared to experimental values of U , the closeness with which the observed points fitted the curve given by equation (2.7) was remarkable. Note that in this equation, R_C is the radius of curvature of the spherical part of the bubble, (not to be confused with the radius R_b of the initial spherical bubble).

2.4.2 Simulations

In order to use Taylor's results as a means of validation, the exact same experimental conditions that were used by the author were chosen for a reliable simulation of the article. The experiments conducted were carried out with air bubbles in water and in nitrobenzene. For the sake of simplicity, the simulations made in this work were only in water. Regarding the boundary conditions, the simulation was done in an infinite medium.

Volume [cm]	Radius [cm]	Ga	Bo
1.5	0.71	2099.62	6.76
2	0.78	2424.43	8.20
2.5	0.84	2710.6	9.52
10	1.33	5421.2	23.98
50	2.28	12122.2	70.11
100	2.88	17143.3	111.29
200	3.63	24244.3	176.673

Table 2.2: Galilei and Bond values for different Taylor bubbles.

Therefore, several parameters can already be set. Considering water as medium 1 and air as medium 2, the densities are $\rho_1 = 997 \text{ kg/m}^3$ and $\rho_2 = 1.225 \text{ kg/m}^3$; and the viscosities are $\mu_1 = 8.90 \times 10^{-4} \text{ Pa} \cdot \text{s}$ and $\mu_2 = 1.81 \times 10^{-5} \text{ Pa} \cdot \text{s}$. In addition, there is the surface tension between these two media $\sigma = 7.286 \times 10^{-2} \text{ N/m}$, and the gravity value $g = 9.81 \text{ m/s}^2$.

In view of these values, it is already possible to fix two of the four dimensionless parameters: $\rho_R = 813.878$ and $\mu_R = 49.171$.

The only dimensional parameter that was consistently tested for multiple values in the Taylor studies was the bubble radius, which was validated for volumes from 1.5 cm^3 up to 200 cm^3 . By fixing some radius values included in this scope, we have the Galilei and Bond values found in Table 2.2.

It is possible to see that the values for the Galilei number substantially exceed the scope studied by the Tripathi phase plot. Analyzing these values, it is reasonable to intuit that the dynamics to be observed by the simulations will probably approach regimes IV or V.

In fact, this intuition is correct and there will be substantial problems in maintaining the bubble's structure. After a certain limit, all bubbles simulated under these conditions will present a central breakup.

Partial Validation of Taylor Bubbles

A first comparison that can be made to better understand the nature of the results is to analyze the emergence of the rupture. For Figs. 2.9, the first three rows of Table 2.2 were taken. Each image was saved at the exact instant when the lowest point on the bubble is as close as possible to the highest point on the axis of symmetry.

From this quick analysis, it is concluded that bubbles with a volume of 2.5 cm^3 are no longer validated by the numerical implementation carried out in this work so far.

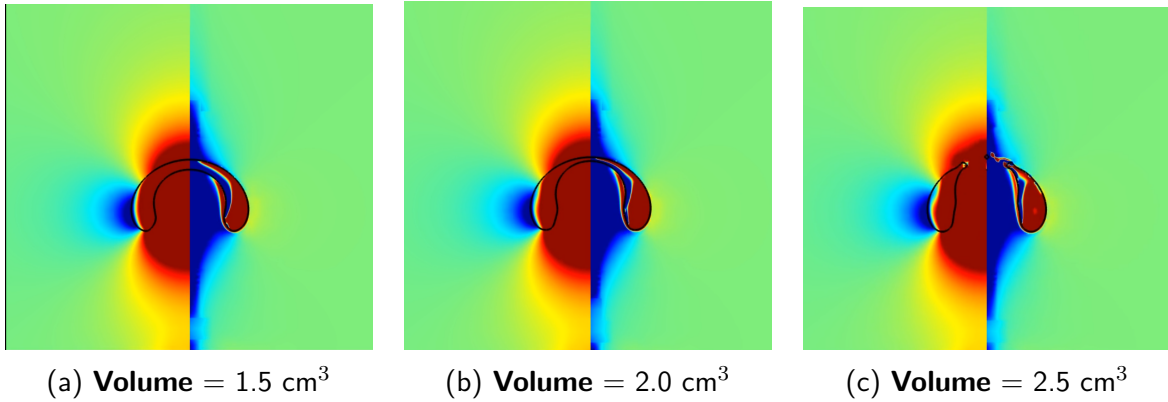


Figure 2.9: Taylor bubbles in transient regime. Snapshots captured at the moment of greatest bubble distension. Vertical velocity on the left and vorticity field on the right.

It is interesting to denote that the nature of the bubble in Fig. 2.9b is practically on the threshold that separates the expected dynamics for Taylor bubbles and the dynamics that present the central breakup. This fact is reinforced by the plot in Fig. 2.10, which shows the position of the lowest and highest point of the bubble on the axis of symmetry. At time $t_u = 0.8$, it is evident that there is a maximum proximity between these ends of the bubble; this setting becomes unstable for subtle increases in Galilei and Bond numbers.

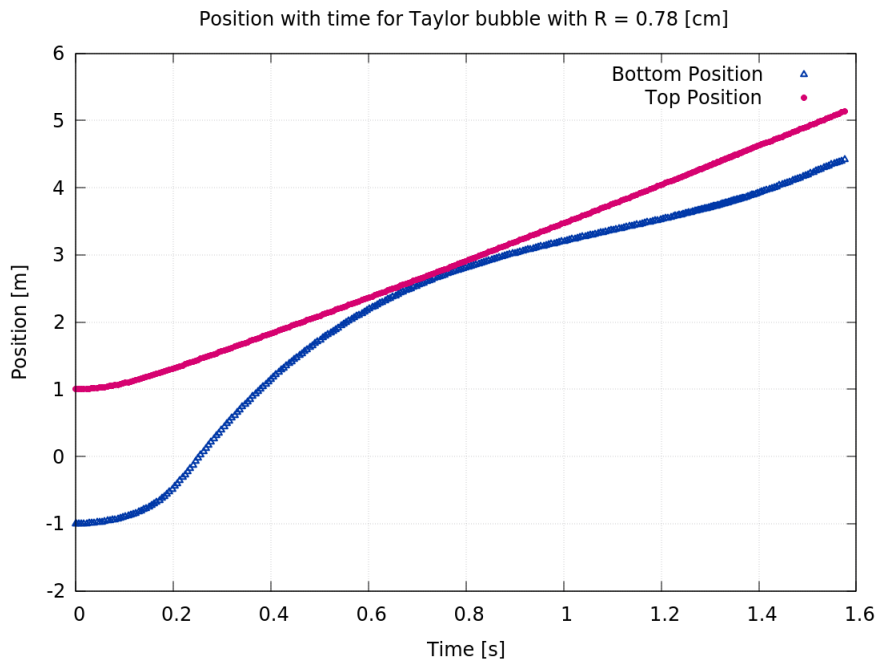


Figure 2.10: Position of the lowest and highest point of the bubble on the axis of symmetry for Taylor bubble with **Volume** = 2.0 cm³.

Despite this, all simulated bubbles that did not show central breakup presented results in agreement with Taylor's theory. This can be clearly seen through Figs. 2.11a and 2.11b, which, after the transient behavior, present a qualitatively similar shape to the classic Taylor bubbles. Furthermore, in Fig. 2.12 there is a comparison between Taylor's analytical terminal velocity, obtained by equation (2.7); with the velocities of the top of the bubbles, obtained through the simulation, and with R_C the radius of curvature obtained from the simulations

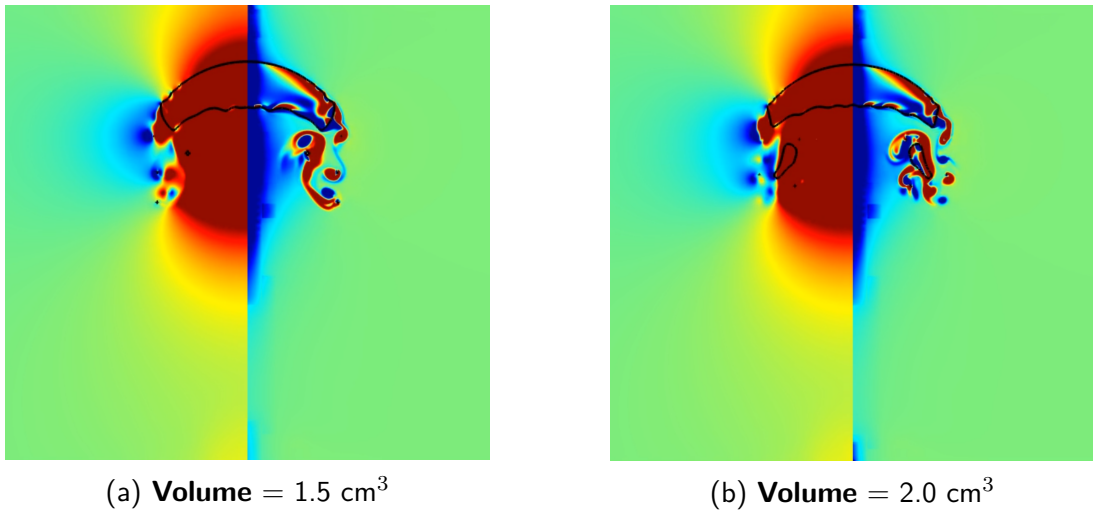


Figure 2.11: Classic Taylor bubbles after transient regime.

In view of the aforementioned information, it is necessary to make some comments about the discrepancy between experiment and simulation. First, a key point is the fact that all simulations performed in this work are axisymmetric in nature. As discussed in section (1.3.3), there are several asymmetric behaviors and patterns that can be observed in different bubble rise regimes. Given this, the axisymmetric simulation already presents a simplification of the real phenomenon.

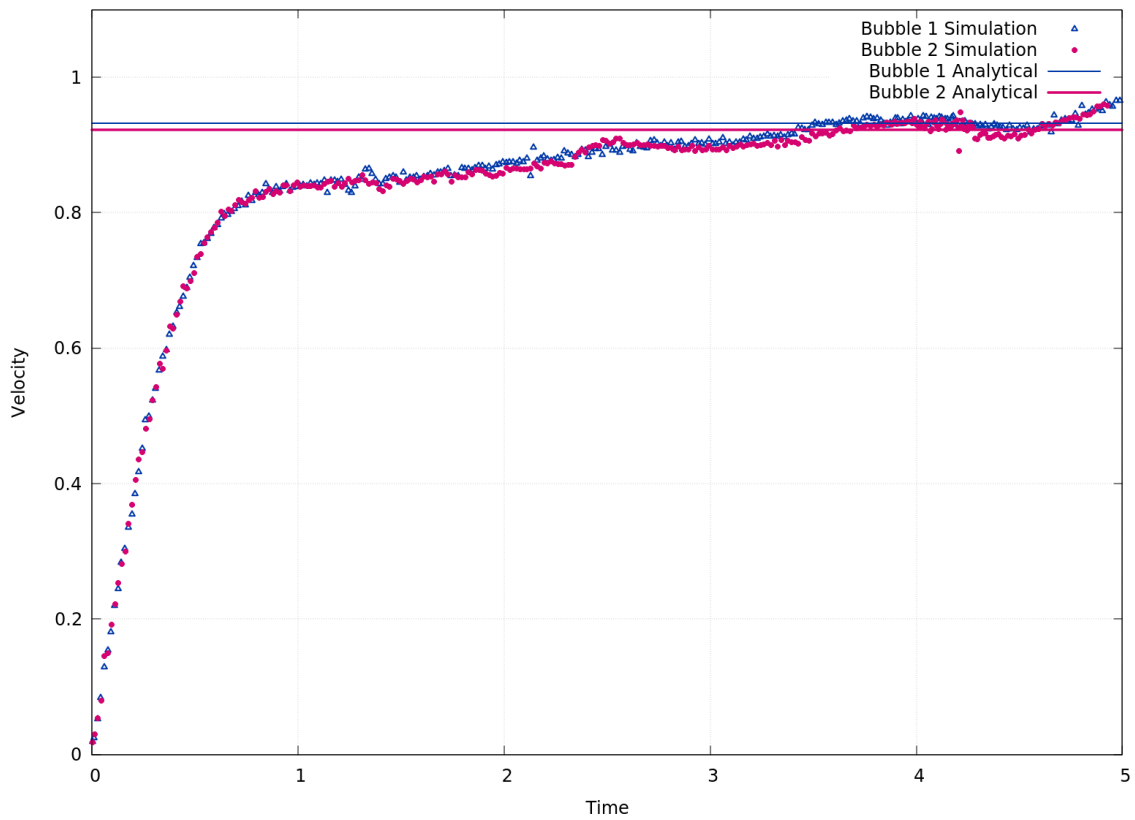


Figure 2.12: Nondimensional comparison between analytical and numerical solution for validated Taylor bubbles. For simplicity, Bubble 1 has **Volume** = 1.5cm³ and Bubble 2 has **Volume** = 2.0cm³.

Additionally, it is interesting to compare the order of magnitude of the Bond and Galilei numbers that were used in the 3D Tripathi simulations in the V regime (which generates toroidal bubbles, with central breakup), with the values obtained for the Taylor experiment. It is possible to notice that the Galilei and Bond values for Taylor bubbles are already considerably higher than the values used by Tripathi for bubbles with a central breakup. That is, even in 3D simulations, it's no wonder that such large numbers of Galilei and Bond trigger such dynamics.

Finally, it is relevant to think about the abrupt nature of imposing constant values for the Galilei number, Bond and for gravity in the numerical domain. In several contexts throughout this work, the sensitivity to the initial conditions that bubbles present has already been discussed (subsection 1.3.3); and the different dynamics that can occur due to details in setup. This indicates that a possible solution to the problem is to make some of the physical parameters that are imposed under the bubble vary smoothly up to a certain point. This approach is the subject of the next subsection.

Varying Gravity Approach

As discussed, in an attempt to more smoothly vary the physical parameters under which the bubble is subjected, one of the solutions is to make gravity vary smoothly until reaching the reference value. Equation (2.8) was chosen to enable this smooth transition.

$$g(t) = \begin{cases} \frac{g_0}{2} \left(1 - \cos\left(\frac{\pi t}{t_u}\right)\right) & \text{if } t \leq t_u \\ g_0 & \text{if } t > t_u \end{cases} \quad (2.8)$$

Among the pertinent parameters of this equation, there is the reference value for gravity g_0 , the same one that is used after the equations are dimensionless. In addition, there is the time t_u , from which the severity remains constant at its reference value g_0 .

Among several attempts, the following methodology was selected as the most suitable to find robust results :

- Perform a simulation with constant gravity as before.
- Find the exact time at which central breakup occurs.
- Use the time found as t_u in equation (2.8), and redo the simulation by varying the gravity according to the equation.

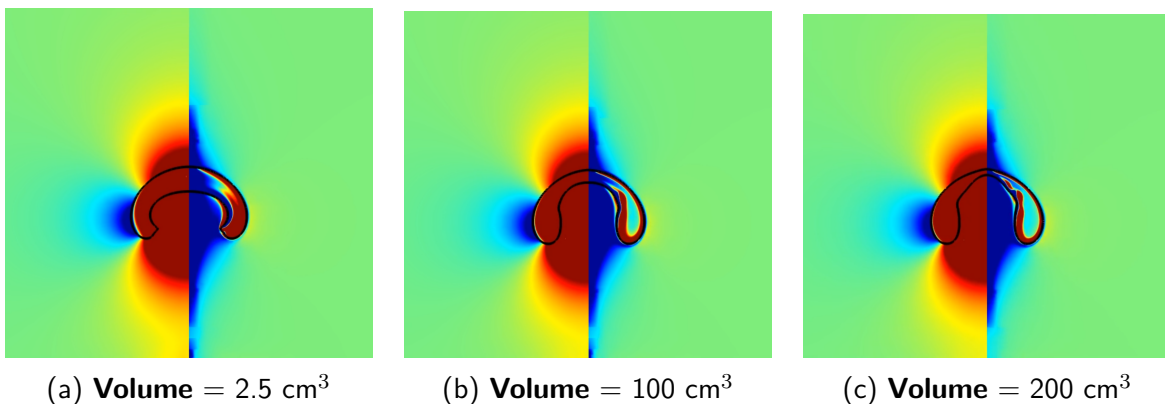


Figure 2.13: Taylor bubbles in transient regime, with varying gravity. Snapshots captured at the moment of greatest bubble distension. Vertical velocity on the left and vorticity field on the right. No central breakup is reported.

From a purely qualitative perspective, it is already remarkable that the peripheral breakup can be avoided in the simplest bubbles that already had this problem, such as the bubble of **Volume** = 1.5 cm^3 (Fig. 2.9c with breakup, and Fig. 2.13a with varying gravity). But more surprising, the method works in all bubbles considered by Taylor's theory, reaching up to 200 cm^3 .

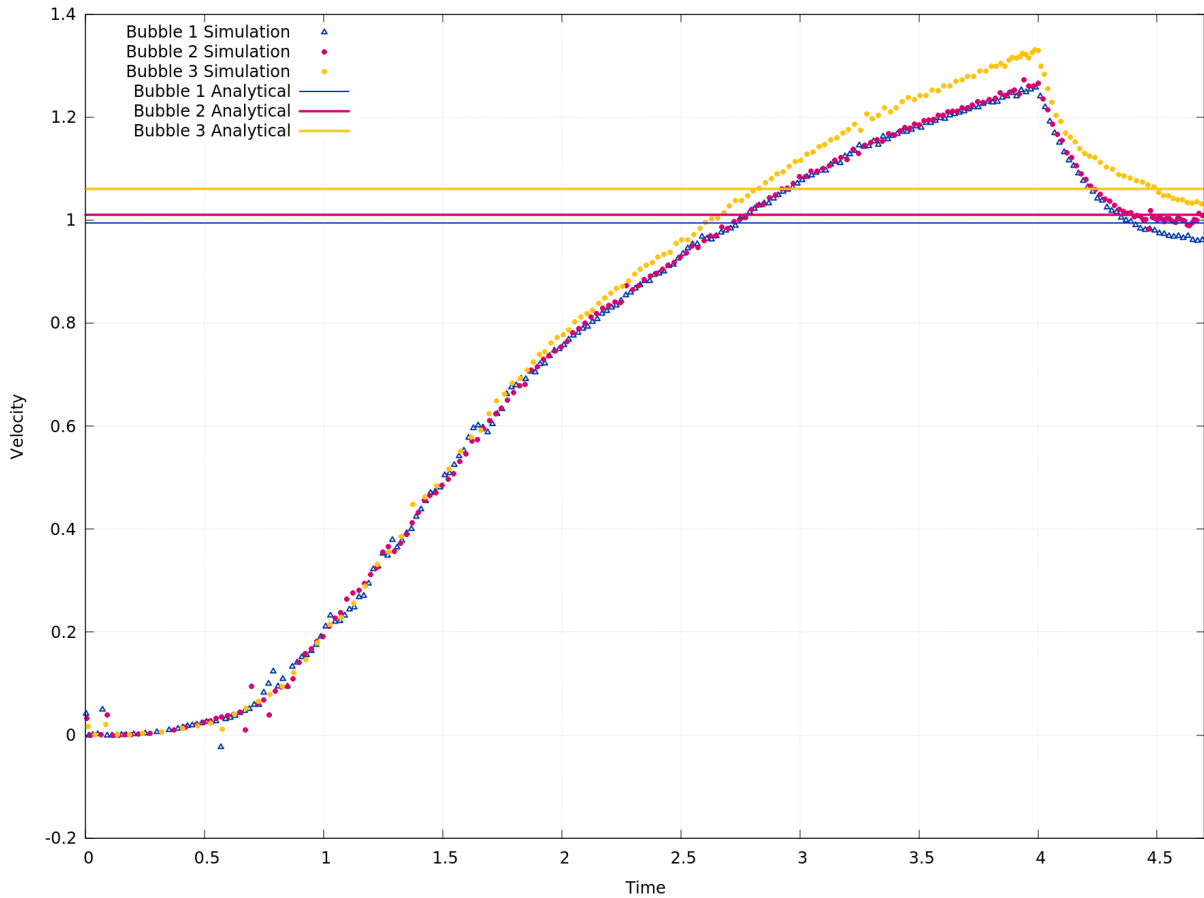


Figure 2.14: Nondimensional comparison between analytical and numerical solution for Taylor bubbles with varying gravity. For simplicity, Bubble 1 has **Volume** = 1.5 cm^3 , Bubble 2 has **Volume** = 100 cm^3 , and Bubble 3 has **Volume** = 200 cm^3 .

Furthermore, the analytical equation proposed by Taylor remains valid and agrees with the simulation results, as can be seen in Figure 2.14.

This fact indicates that the only problem that needed to be worked around is the peripheral breakup that can occur due to abrupt initial conditions (such as high Galilei and Bond numbers). By smoothly varying the gravity, the physical nature of the problem is not readily imposed; being able to overcome any unwanted transient behavior and remaining faithful to the original dynamics in the steady state.

Part 3

Varying Gravity

3.1 Introduction

This part of the work is devoted to a concrete reorientation study. It consists of the analysis of motion of gas/vapor bubbles rising inside the column of liquid. Typically, the bubble occupy around 20-80 % the container volume.

The relevance of this study, from an application perspective, is the optimization of the performance of a liquid propulsion rocket system. that is destined to launch multiple satellites in orbits around earth. Several restarts with intermediate phases of coasting are required, and at the end of each coasting phase it is necessary to ensure that the liquid propellant will be available near the inlet of the engine. The position of the liquid propellant inside the rocket tank at the end of the coasting phase is however unknown, and is dictated by various factors like the orbit manoeuvres, orbital perturbations, start and shut-down transients etc. It is thus important to apply a small acceleration (called reorientation acceleration) to collect the propellant at the inlet of the engine. This acceleration, if large enough, can cause the liquid propellant to rebound from the bottom end of the reservoir and reorient itself to form a geyser, thus limiting the amount of liquid collected near the engine inlet pipe.

At first, some details of Gandikota's study [21] will be presented, which focuses centrally on this theme. Then, comparative simulations will be made with his work.

3.2 Gandikota's Experiment

Experiments are carried out using the facility OLGA (Oxygen Low Gravity Apparatus), which has the capability of realizing experiments with a very fast variation of gravity (using a strong magnetic field), from zero-g to 0.4g in a cell filled with oxygen. Oxygen is affected by the magnetic field due to its paramagnetic nature. In this subsection, only the relevant aspects for the simulation of bubbles will be dealt with. For more technical details about the device and the generation of the magnetic field, see [21].

Under these conditions, the physical properties of liquid and vapor oxygen are shown below. The subscripts L and V correspond to the liquid and vapor phases.

- Densities $\rho_L = 1142 \text{ kg/m}^3$ and $\rho_V = 1.963 \text{ kg/m}^3$
- Viscosities $\mu_L = 1.96 \times 10^{-4} \text{ Pa} \cdot \text{s}$ and $\mu_V = 7 \times 10^{-6} \text{ Pa} \cdot \text{s}$
- Liquid-vapor surface tension $\sigma = 1.32 \times 10^{-2} \text{ N/m}$

Regarding the bubbles used in the experiment, due to the influence of the magnetic field used, they are initially ellipsoidal, as shown in Fig. 3.1 (explanation for this phenomenon can be found in [22]). Furthermore, h and d values are 100 mm and 30 mm, respectively.

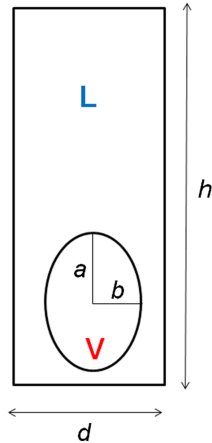


Figure 3.1: Computational domain for 2D numerical simulation. Source: Gandikota [21]

In addition, two main bubbles were used in the experiment. Information regarding them can be found in Table 3.1. Zero-g conditions are setup inside the cell by energizing the solenoid. The bubble is levitated initially with its center at a distance of around 20 mm from the bottom of the cell. The gravity quench is simulated by suddenly discharging the inner solenoid to 0 A, which takes place with a time constant of around 340 ms (as shown in Fig. 3.2). The effective gravity inside the cell is ideally supposed to change from 0g to 0.4g with a time constant of 320 ms.

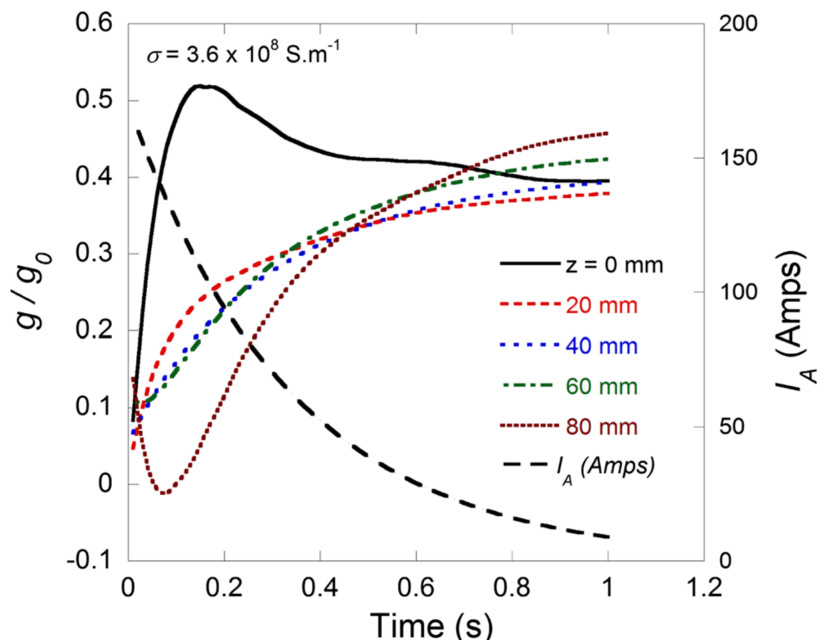


Figure 3.2: Spatio-temporal variation of the gravity field inside the cell and variation of the current (I_A). Source: Gandikota REFFF

	Semi-major axis (mm)	Semi-minor axis (mm)	Bubble Volume (mm ³)	Fill Ratio (%)
Bubble 1	13.5	8.5	4100	5.9
Bubble 2	16.5	12.5	10750	15.3

Table 3.1: Bubble sizes and fill ratios used for the experiments. Source: Gandikota [21]

3.3 Simulations

2D numerical simulations were carried out by Gandikota, firstly to compare the results with experiments and then to further extend the scope of his work. The general Volume of Fluid (VOF) approach was used, where a local phase volume fraction was introduced to capture the interface. Furthermore, the method of VOF-PLIC (piecewise linear interface calculation) was employed, which is a volume-preserving scheme with geometric reconstruction of the interface.

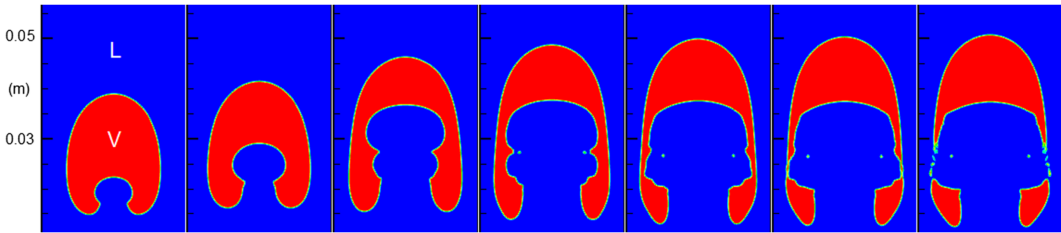


Figure 3.3: Bubble 1 snapshots at selected times: 0.09 s, 0.12 s, 0.18 s, 0.21 s, 0.225 s, 0.23 s, 0.235 s. Source: Gandikota [21]

In Fig. 3.3, the results obtained by the simulation for bubble 1 can be seen. The focus of the snapshot sequence is to show the evolution of the geyser and how this ultimately leads to the peripheral breakup of the bubble.

Surprisingly, the simulation performed does not take into account the variation in gravity, with only an imposition of 0.4g as an initial condition. The author recognizes that in fact this is an oversimplification of the experimental setup, but that this will only distance his simulation from the initial moments of the bubble's dynamics, when the variation in gravity is more significant. Also, he mentions the difficulty of running a simulation with such a level of complexity.

Having said that, the dimensionless numbers for the Gandikota simulation are:

- Densities ratio $\rho_R = 581.763$
- Viscosities $\mu_R = 28$
- Galilei numbers $Ga_1 = 11418.8$ and $Ga_2 = 18489.9$
- Bond numbers $Bo_1 = 33.4671$ and $Bo_2 = 63.6357$

Still considering the discussions made in Section 1.3.3, it is valid to question the choices made by the author in order to reliably simulate the experimental phenomenon. The discrepancy from the real physical nature of the phenomenon by the use of axisymmetric simulations instead of 3D has already been discussed. 2D simulations only increase this contrast further, especially for a high Galilei and Bond regime.

Finally, using the same setup as the Gandikota's simulation (2D), the results of this work can be seen in Fig. 3.4. In it, snapshots were taken at the same instants of Fig. 3.3.

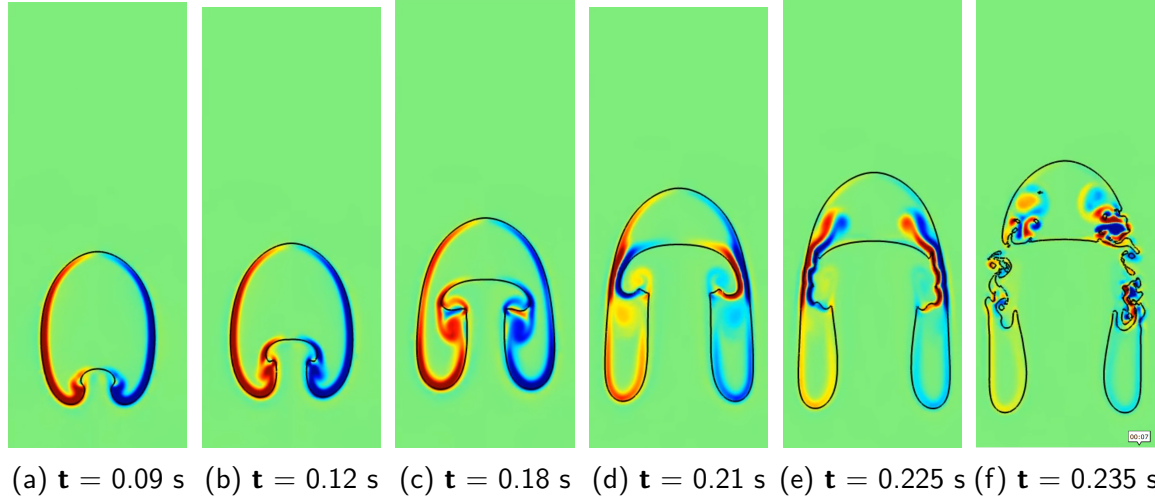


Figure 3.4: Bubble 1 snapshots at selected times for comparison.

It is noticeable that there are contrasts between both simulations, mainly in the exact structure of the geyser, which seems to be distributed more in the lower part of the bubble in the first moments. On the other hand, the qualitative dynamics of the bubbles and the exact moment of peripheral breakup were in agreement. The other variations can be explained by the formulations and methods used in each simulation.

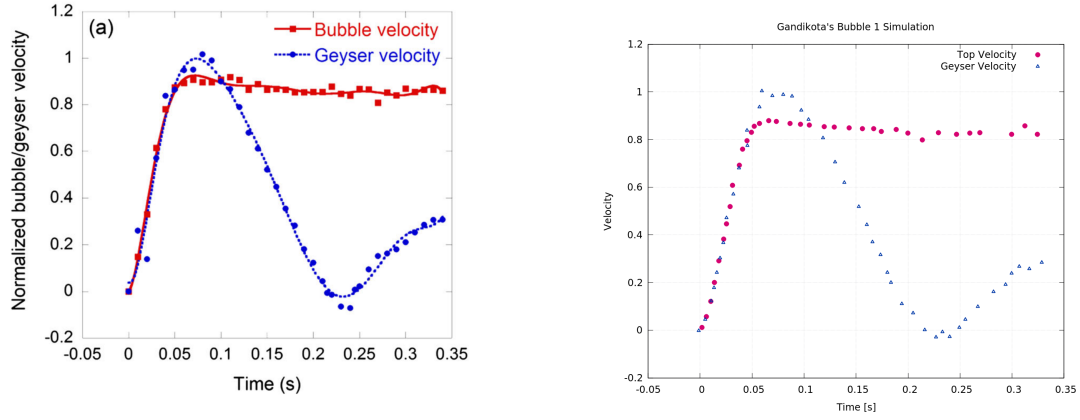


Figure 3.5: Velocity comparison between simulations. Velocity was left nondimensionalized.

Furthermore, a comparative plot was made with the results of Gandikota, as can be seen in Fig. 3.5. Only time was dimensioned in order to provide a physical understanding of the duration of the real phenomenon. It is interesting to note the qualitative agreement between the curves, with the geyser velocity reaching a maximum and returning before the peripheral breakup.

Part 4

Added Mass

4.1 Introduction

This final part of the work is devoted to the study of the influence of added mass on the rise of bubbles. First, the concept of added mass and how it fits into the mathematical formulation of the rise of a bubble will be introduced. Then, quick validations will be done with the content already developed in this work. And finally, a study will be made of the influence of added mass in physical scenarios that are beyond the scope of studies already developed. The first analysis will consist of how the added mass behaves in face of gradual confinement effects. The second will focus on how it behaves when facing bubbles with different eccentricities. The purpose of these analyzes is to unravel the effects that underlie the dynamics of bubbles in Gandikota's experiments, seen in Part 3.

4.2 Theory

4.2.1 Physical Perspectives

Despite its presence in many trivial physical contexts, added mass is commonly not discussed. One of the reasons for this, as Pantaleone [23] points out, is the fact that there are few discussions of it in the research literature. Most examinations of the forces on an object moving through a fluid treat motion at constant velocity, what are called the "steady" forces. The additional forces that are present when an object's velocity is not constant are called the "unsteady" forces. The "unsteady" forces are more difficult to measure and the few existing measurements involve either free-fall of a sphere (or bubble) released from rest or a sphere in oscillatory motion. The unsteady forces are unexplored for a typical ball moving through the air.

In order to physically explain the concept of added mass, let us consider a large, light spherical ball (such as an inflatable beach ball) is gently tossed into the air. As the ball accelerates, it must also accelerate the air around it. Thus a ball moving through air has a larger effective inertia than one moving through vacuum. This increase in inertia also reduces the acceleration from the force of gravity acting on the ball. The increase in inertia of an object moving through a fluid is usually called **added mass**.

$$\underbrace{-F\vec{u}}_{\text{Rate of Additional Work}} = \underbrace{\frac{dK}{dt}}_{\text{Rate of Kinetic Energy}} \quad (4.1)$$

4.2.2 Added Mass for Bubble Ascension

In view of the aforementioned concepts, the motion equation for a sphere composed of fluid 2, moving through fluid 1, is:

$$m \frac{d\overrightarrow{\mathbf{u}}(t)}{dt} = F_{Buoyancy} - F_{Weight} - F_{Drag} - F_{Added\ Mass} \quad (4.2)$$

As this equation is valid only for spheres, it will be valid for the bubble only in the initial moments of its motion. This does not present problems for the study of the added mass, since its moment of greatest influence is precisely at the beginning of the dynamics, when the bubble is accelerating and has not yet been deformed. Putting each force according to the physical variables of relevance:

$$\frac{4}{3}\pi R_b^3 \rho_2 \frac{d\overrightarrow{\mathbf{u}}(t)}{dt} = \frac{4}{3}\pi R_b^3 (\rho_1 - \rho_2) g(t) - \frac{1}{2}\rho_1 \pi R_b^2 C_D \overrightarrow{\mathbf{u}}(t)^2 - \frac{4}{3}\pi R_b^3 \rho_1 C_m \frac{d\overrightarrow{\mathbf{u}}(t)}{dt} \quad (4.3)$$

Where R_b the radius of the bubble, $g(t)$ the local gravity, C_D the friction coefficient and C_m the added mass coefficient. Both C_m and C_D coefficient are dependent on the bubble shape and confinement. Then, organizing this equation:

$$\frac{4}{3}\pi R_b^3 (\rho_2 + C_m \rho_1) \frac{d\overrightarrow{\mathbf{u}}(t)}{dt} = \frac{4}{3}\pi R_b^3 (\rho_1 - \rho_2) g(t) - \frac{1}{2}\rho_1 \pi R_b^2 C_D \overrightarrow{\mathbf{u}}(t)^2 \quad (4.4)$$

In the acceleration term of equation (4.4), the added mass coefficient C_m comes from the unsteady displacement of the fluid by the bubble motion. The value of this coefficient can be shown analytically to be $C_m = 0.5$ for a solid sphere, using potential flow theory [19].

However, by focusing the study on a strictly transient regime, for short times, the friction force will be negligible because the bubble has not reached considerable speeds:

$$\frac{4}{3}\pi R_b^3 (\rho_2 + C_m \rho_1) \frac{d\overrightarrow{\mathbf{u}}(t)}{dt} = \frac{4}{3}\pi R_b^3 (\rho_1 - \rho_2) g(t) \quad (4.5)$$

Also, noting that $\rho_1 \gg \rho_2$:

$$\frac{d\overrightarrow{\mathbf{u}}(t)}{dt} = \frac{1}{C_m} g(t) \quad (4.6)$$

Considering equation (4.6), and the information that $C_m = 0.5$ for spherical bubbles [19]; we conclude that it is always expected to obtain as acceleration of the bubble twice the value of the imposed gravity. As many of the analyzes and graphs performed in this work remain in the dimensionless numerical domain, it is expected to find the value of initial acceleration of the bubble as 2.

4.3 Simulations

4.3.1 Constant vs Varying Gravity

As discussed in the previous subsection, a first validation of relevance is the simulation of a simple spherical bubble in an infinite medium with the imposition of a constant gravity. For reasons of simplicity, the physical nature of the chosen bubble approximates to a Taylor bubble.

Therefore, the following values for the dimensionless numbers follow:

- Density ratio $\rho_R = 800$
- Viscosity ratio $\mu_R = 50$
- Galilei number $Ga = 2000$
- Bond number $Bo = 7$

As the dimensionless gravity imposed in the numerical scope is equivalent to 1, we are expected to obtain acceleration values close to 2, according to the equation (4.6). As can be seen in Fig. 4.1, the simulation is in agreement with the additional mass theory in considering the bubble as a spherical object in the first few moments.

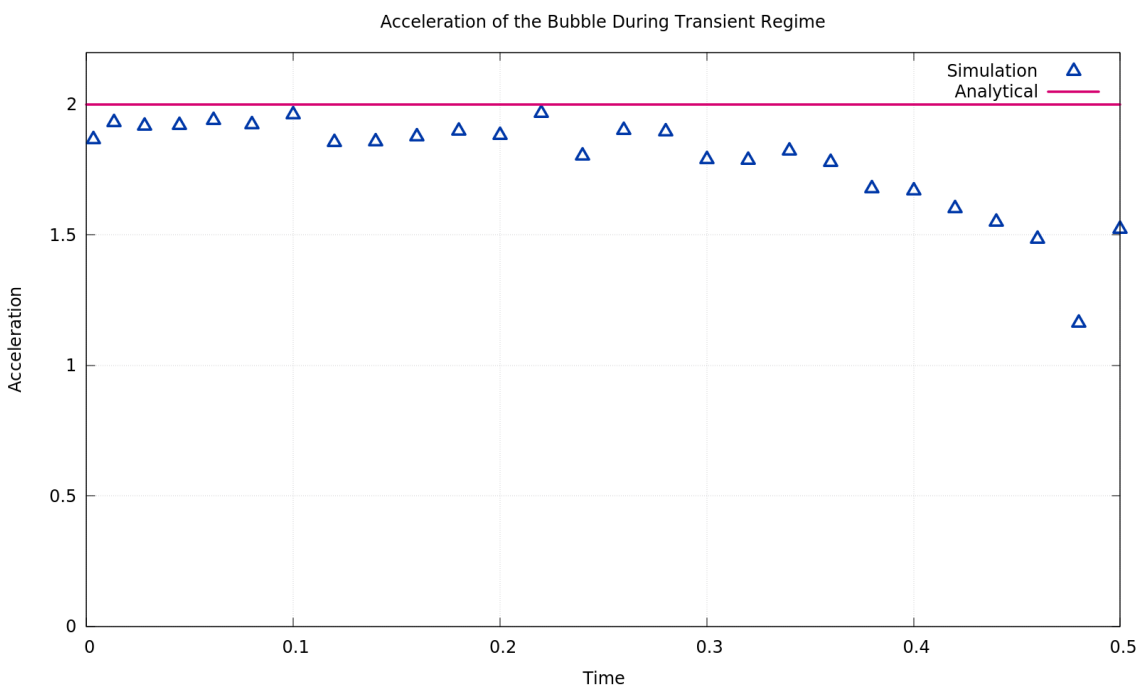


Figure 4.1: Acceleration of simple spherical bubble.

4.3.2 Aspect Ratio Study

In order to study this influence, 6 simulations were performed; of which one is simulated in an infinite domain and the rest is gradually more confined. The values used for each simulation can be seen in Table 4.1.

	Radius	Ratio $\frac{r}{h}$
Bubble 1	4	0.5
Bubble 2	3.5	0.4375
Bubble 3	3	0.375
Bubble 4	2.5	0.3125
Bubble 5	2	0.25

Table 4.1: Ratio values corresponding to each simulated bubble.

As can be seen in Fig. 4.2, there is a significant qualitative change as bubbles ascend into more confined domains. All images were taken at the same time and under the same physical conditions. It is possible to notice that the geyser formation at the bottom of the bubble increases as the bubble becomes more confined, at first. But in more extreme conditions of confinement, there may be premature peripheral rupture, as in Fig. 4.2e.

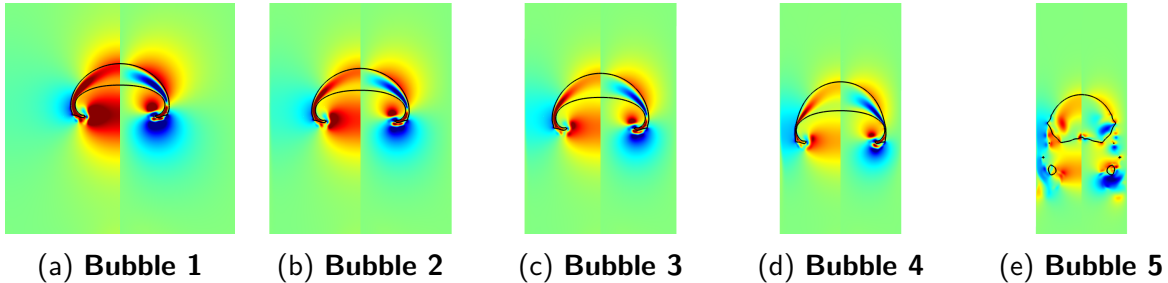


Figure 4.2: Comparison between bubble rises at different confinement ratios. The color gradient represents the vertical and horizontal velocity, on the right and on the left, respectively.

Even more interesting, when analyzing how the acceleration values behave for each bubble, in Fig. 4.3, it can be seen that confinement implies a decrease in acceleration; that is, an increase in the added mass coefficient C_m .

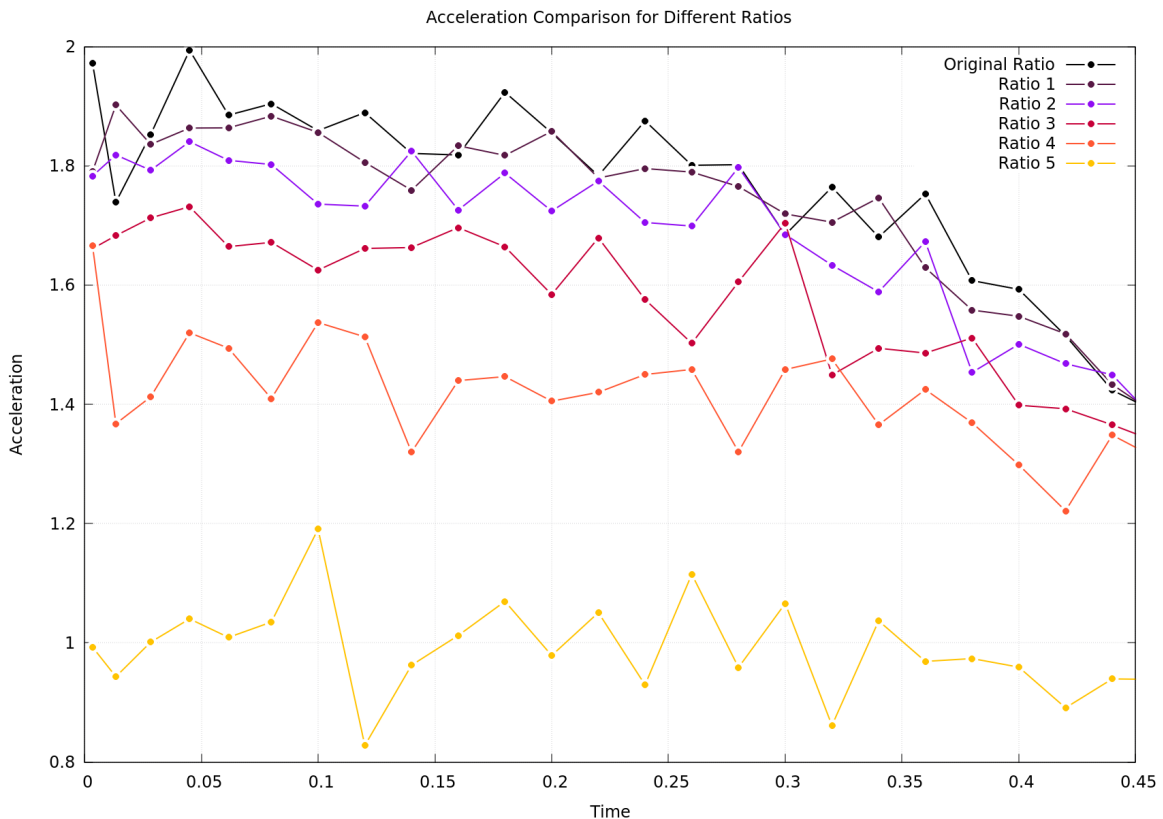


Figure 4.3: Nondimensional acceleration comparison between bubble rises at different confinement ratios.

This fact makes sense from a physical perspective, since closer proximity to the walls implies a greater influence of the boundary layer on bubble dynamics. Another way of thinking

is that the bubble needs to deliver more energy to the surrounding fluid in order to accelerate it as it would without confinement.

4.3.3 Eccentricity Study

Another particular feature of the bubbles in Gandikota REF's experiment was the fact that they were not spherical but rather ellipsoidal.

As the confinement was studied, 5 bubbles of different eccentricities were selected in order to analyze how their acceleration behaves in an infinite medium. Information for each bubble can be found in Table 4.2.

	Major Axis	Minor Axis	Eccentricity
Bubble 1	1.052	0.958	0.413
Bubble 2	1.104	0.916	0.558
Bubble 3	1.156	0.874	0.654
Bubble 4	1.208	0.832	0.725
Bubble 5	1.26	0.79	0.779

Table 4.2: Eccentricity values corresponding to each simulated bubble.

As can be seen in Fig. 4.4, unlike the influence of confinement, the more elliptical the bubbles initially, the greater the acceleration. That is, the smaller the additional mass coefficient C_m will be.

From a physical perspective, this fact can be explained by a greater distribution of the bubble's mass along the upward direction.

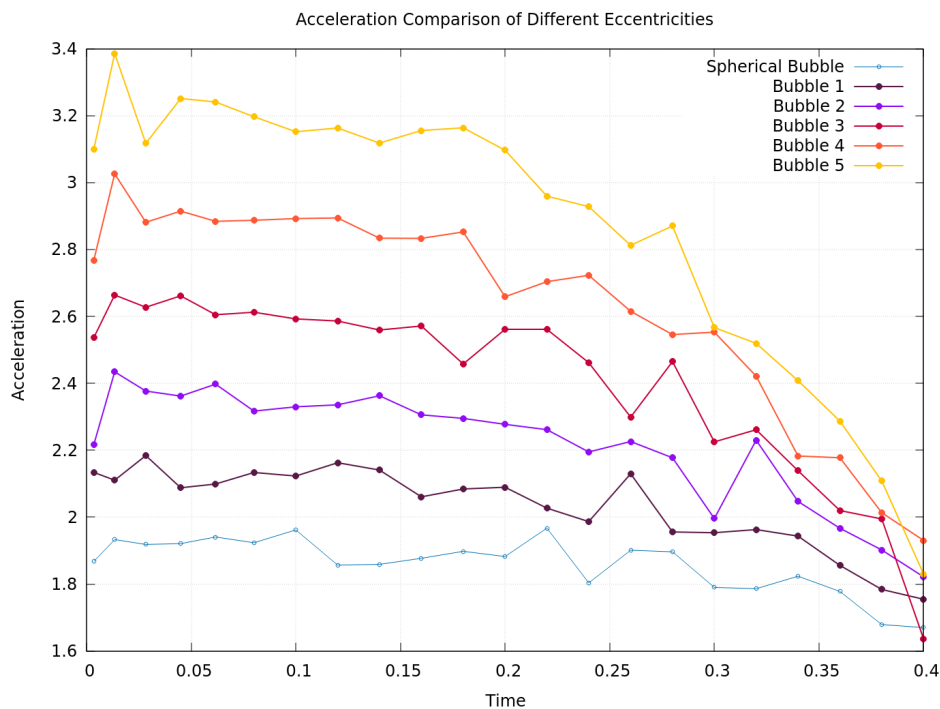


Figure 4.4: Nondimensional acceleration comparison between bubble rises at different eccentricities.

Part 5

Conclusion

In a review of all the facts presented in this work, it was possible to study different dynamics of bubble rise as a function of 4 dimensionless numbers, with the help of the open-source tool, Basilisk. Additionally, Gandikota's work [?] with variable gravity was presented, validated and served as the basis for further analyzes focused on the nature of the added mass force.

Consecutively, three pillars of simulation validation were presented: Stokes flow, Tripathi phase diagram and Taylor bubbles. Only in the latter were there divergences between the standard methodology, in view of the central breakup.

Furthermore, in view of the asymmetrical physical nature of the bubbles in some regimes, discrepancies and insufficiencies of 2D and axisymmetrical simulations with respect to 3D were denoted. Particularly in this question, a method capable of avoiding the central breakup in axisymmetric simulations with high values of the Galilei and Bond numbers was presented.

From a holistic perspective, the work was able to achieve its goals, deal with unforeseen results and circumvent them.

Bibliography

- [1] Manoj Kumar Tripathi, Kirti Chandra Sahu, and Rama Govindarajan. Dynamics of an initially spherical bubble rising in quiescent liquid. *Nature Communications*, 2015.
- [2] Christian Veldhuis, Arie Biesheuvel, and Leen Van Wijngaarden. Shape oscillations on bubbles rising in clean and in tap water. *Physics of fluids*, 20(4):040705, 2008.
- [3] JC Cano-Lozano, P Bohorquez, and C Martínez-Bazán. Wake instability of a fixed axisymmetric bubble of realistic shape. *International journal of multiphase flow*, 51:11–21, 2013.
- [4] Kamil Wichterle, Marek Večeř, and Marek Ržička. Asymmetric deformation of bubble shape: cause or effect of vortex-shedding? *Chemical Papers*, 68(1):74–79, 2014.
- [5] AWG De Vries, A Biesheuvel, and L Van Wijngaarden. Notes on the path and wake of a gas bubble rising in pure water. *International journal of multiphase flow*, 28(11):1823–1835, 2002.
- [6] Thomas Bonometti and Jacques Magnaudet. Transition from spherical cap to toroidal bubbles. *Physics of Fluids*, 18(5):052102, 2006.
- [7] JR Grace, T Wairegi, and J Brophy. Break-up of drops and bubbles in stagnant media. *The Canadian Journal of Chemical Engineering*, 56(1):3–8, 1978.
- [8] Julien R Landel, Carlo Cossu, and CP Caulfield. Spherical cap bubbles with a toroidal bubbly wake. *Physics of Fluids*, 20(12):122101, 2008.
- [9] John B Bell, Phillip Colella, and Harland M Glaz. A second-order projection method for the incompressible navier-stokes equations. *Journal of computational physics*, 85(2):257–283, 1989.
- [10] Nikolaos D. Katopodes. Chapter 12 - volume of fluid method. In Nikolaos D. Katopodes, editor, *Free-Surface Flow*, pages 766–802. Butterworth-Heinemann, 2019.
- [11] Stéphane Popinet. Gerris: a tree-based adaptive solver for the incompressible euler equations in complex geometries. *Journal of computational physics*, 190(2):572–600, 2003.
- [12] Stéphane Popinet. An accurate adaptive solver for surface-tension-driven interfacial flows. *Journal of Computational Physics*, 228(16):5838–5866, 2009.
- [13] P-Y Lagrée, Lydie Staron, and Stéphane Popinet. The granular column collapse as a continuum: validity of a two-dimensional navier–stokes model with a μ (i)-rheology. *Journal of Fluid Mechanics*, 686:378–408, 2011.

BIBLIOGRAPHY

- [14] Marsha J Berger and Phillip Colella. Local adaptive mesh refinement for shock hydrodynamics. *Journal of computational Physics*, 82(1):64–84, 1989.
- [15] William John Coirier. *An adaptively-refined, Cartesian, cell-based scheme for the Euler and Navier-Stokes equations*. PhD thesis, University of Michigan, 1994.
- [16] Louis H Howell and John B Bell. An adaptive mesh projection method for viscous incompressible flow. *SIAM Journal on Scientific Computing*, 18(4):996–1013, 1997.
- [17] J Antoon Van Hooft, Stéphane Popinet, Chiel C Van Heerwaarden, Steven JA Van der Linden, Stephan R de Roode, and Bas JH Van de Wiel. Towards adaptive grids for atmospheric boundary-layer simulations. *Boundary-layer meteorology*, 167(3):421–443, 2018.
- [18] Stéphane Popinet. A quadtree-adaptive multigrid solver for the serre–green–naghdi equations. *Journal of Computational Physics*, 302:336–358, 2015.
- [19] Horace Lamb. *Hydrodynamics*. University Press, 1924.
- [20] Ro Mo Davies and Geoffrey Ingram Taylor. The mechanics of large bubbles rising through extended liquids and through liquids in tubes. *Proceedings of the Royal Society of London. Series A. Mathematical and Physical Sciences*, 200(1062):375–390, 1950.
- [21] G Gandikota, Guillaume Pichavant, Denis Chatain, Sakir Amiroudine, and Daniel Beysens. Geyser formation in oxygen when subjected to fast acceleration changes. *Microgravity Science and Technology*, 27(2):115–127, 2015.
- [22] Jérôme Duplat and Alain Mailfert. On the bubble shape in a magnetically compensated gravity environment. *Journal of Fluid Mechanics*, 716, 2013.
- [23] J Pantaleone and J Messer. The added mass of a spherical projectile. *American Journal of Physics*, 79(12):1202–1210, 2011.
Possible numerical method used in basilisk Bonometti, T. Magnaudet, J. An interface-capturing method for incompressible two-phase flows. validation and application to bubble dynamics. Int. J. Multiphase Flow 33, 109–133 (2007).

List of Tables

2.1	Galilei and Bond numbers used for each simulation based on the rising bubble phase plot.	20
2.2	Galilei and Bond values for different Taylor bubbles.	25
3.1	Bubble sizes and fill ratios used for the experiments. Source: Gandikota [21]	32
4.1	Ratio values corresponding to each simulated bubble.	36
4.2	Eccentricity values corresponding to each simulated bubble.	38

List of Figures

1.1	Different regimes of bubble shape and behaviour. Source: Tripathi et al. [1]	13
1.2	Time evolution of bubbles exhibiting a peripheral and a central breakup. Source: Tripathi et al. [1]	14
1.3	Differences between 2D and 3D bubble simulations from region IV. Source: Tripathi et al. [1]	14
1.4	Schematic of fluid volume fraction and fluid interface. Source: Katopodes [10]	15
1.5	Example of quadtree discretisation and corresponding tree representation. Source: Popinet [11]	16
1.6	Example of octree refinement: snapshots of (a) the vorticity field, and (b) the numerical grid for the lid-driven cavity simulation with $Re_{lid} = 500$. Source: Van Hooft [17]	17
2.1	Snapshots of bubble ascending in Stokes flow. Vertical velocity on the left side and horizontal velocity on the right side.	19
2.2	Comparison between analytical and numerical solution for bubble velocity in Stokes flow. Triangles : Numerical solution. Continuous line : Equation 2.3	20
2.3	Bubble ascending in regime I	21
2.4	Oscillating behavior for bubble ascending in regime II. Vertical velocity on the left side and vorticity field on the right side.	21
2.5	Comparison between regimes III and IV. Vertical velocity on the left side and vorticity field on the right side.	22
2.6	Toroidal bubble ascending in regime V. Vertical velocity on the left side and vorticity field on the right side.	22
2.7	Experimental Taylor bubbles. Source: Davies and Taylor (1950) [20]	23
2.8	Scheme representing pressure variation with respect to the angle θ . Source: Davies and Taylor (1950) [20]	24
2.9	Taylor bubbles in transient regime. Snapshots captured at the moment of greatest bubble distension. Vertical velocity on the left and vorticity field on the right.	26
2.10	Position of the lowest and highest point of the bubble on the axis of symmetry for Taylor bubble with Volume = 2.0 cm ³ .	26
2.11	Classic Taylor bubbles after transient regime.	27
2.12	Nondimensional comparison between analytical and numerical solution for validated Taylor bubbles. For simplicity, Bubble 1 has Volume = 1.5cm ³ and Bubble 2 has Volume = 2.0cm ³ .	27
2.13	Taylor bubbles in transient regime, with varying gravity. Snapshots captured at the moment of greatest bubble distension. Vertical velocity on the left and vorticity field on the right. No central breakup is reported.	28

2.14 Nondimensional comparison between analytical and numerical solution for Taylor bubbles with varying gravity. For simplicity, Bubble 1 has Volume = 1.5cm^3 , Bubble 2 has Volume = 100cm^3 , and Bubble 3 has Volume = 200cm^3 .	29
3.1 Computational domain for 2D numerical simulation. Source: Gandikota [21]	31
3.2 Spatio-temporal variation of the gravity field inside the cell and variation of the current (I_A). Source: Gandikota REFFF	31
3.3 Bubble 1 snapshots at selected times: 0.09 s, 0.12 s, 0.18 s, 0.21 s, 0.225 s, 0.23 s, 0.235 s. Source: Gandikota [21]	32
3.4 Bubble 1 snapshots at selected times for comparison.	33
3.5 Velocity comparison between simulations. Velocity was left nondimensionalized.	33
4.1 Acceleration of simple spherical bubble.	36
4.2 Comparison between bubble rises at different confinement ratios. The color gradient represents the vertical and horizontal velocity, on the right and on the left, respectively.	37
4.3 Nondimensional acceleration comparison between bubble rises at different confinement ratios.	37
4.4 Nondimensional acceleration comparison between bubble rises at different eccentricities.	38